Naturwissenschaftlich-Technische Fakultät

Universität Siegen

UNIVERSITÄT SIEGEN

MASTERARBEIT

Development of a Test System to Probe Beacon-Based sub-ns Synchronization of Autonomous Radio Detectors at the Pierre Auger Observatory

---

Noah Siegemund

Arbeit zur Erlangung des akademischen Grades
Master of Science

vorgelegt der

Experimentellen Teilchen- und Astroteilchenphysik
Department Physik

Gutachter
Prof. Dr. Markus Cristinziani
Prof. Dr. Markus Risse

Betreuer
Dr. Qader Dorosti

7. November 2025

Dieser Forschungsbericht wurde als Masterarbeit von der Naturwissenschaftlich-Technischen Fakultät der Universität Siegen angenommen. Seit der Annahme sind höchstens geringfügige Änderungen vorgenommen worden. Der wissenschaftliche Inhalt der Arbeit ist unverändert.

Angenommen am:	30.09.2025
1. Gutachter:	Prof. Dr. Markus Cristinziani
2. Gutachter:	Prof. Dr. Markus Risse

Contents

CHAPTER 1

Introduction

Nature produces a variety of highly energetic particles that continuously bombard the Earth's atmosphere from outer space. These so-called cosmic rays originate from various sources in the universe and can reach energies above 10^{20} eV. More than 100 years after their discovery in 1912 by Victor Hess, many questions regarding the origin and acceleration mechanisms, as well as the interactions they undergo with molecules in the air of these ultra-high-energy cosmic rays (UHECRs), are not fully understood yet. Hence, they are still an object of current research. UHECRs are studied using the extensive air showers, which are created when the primary particles, protons in most cases, hit the atmosphere of the Earth. These air showers give insights into the fundamental interactions of particles at the highest energies. Large-scale arrays of autonomous detectors are used to measure properties such as incoming direction, particle composition, and the structure of extensive air showers. The largest one, the Pierre Auger Observatory with its water Cherenkov Surface Detector (SD), the Fluorescence Detector (FD), or the Auger Radio Engineering Array (AERA), is located in Argentina. Among the different types of detectors that can be deployed for those types of measurements, radio detectors come with the advantage of large effective coverage for comparatively low costs. In addition, they are capable of operating with a duty cycle close to 100 %. This makes them attractive for scientific experiments in astroparticle physics.

However, to achieve high precision in the reconstruction, an accurate timing of various autonomous detector stations up to 1.5 km apart from each other is needed. Widely used satellite navigation systems like GPS are limited in that sense and can deliver a timing accuracy only up to a range of a few tens of nanoseconds. Exploring new techniques like radio interferometry in air showers requires an increased timing precision to resolve the radio footprint in detail. To tackle this problem, AERA has installed a reference beacon, transmitting well-defined radio signals into the detector array. The beacon signal allows for offline timing corrections in the analysis of air shower data.

In order to verify the ability of the beacon to correct for the timing drifts with an accuracy at the sub-ns level, we developed a dedicated test system based on White Rabbit (WR) technology. The test system enables synchronized data acquisition and data transfer to

probe the beacon synchronization method at different locations. It is designed to verify the beacon-based synchronization technique employed at AERA. The WR network is able to deliver clock signals over a km distance using optical fibers with a precision in the range of picoseconds. This system is used to synchronize the antenna readout of three detector stations via a PPS signal provided by each WR station. The data is analyzed offline using signal processing techniques like cross-correlation and Fourier transformations to determine whether the phase stability of the beacon signal is sufficient to enable interferometric measurements. Data acquisition (DAQ) boards from the AERA experiment were modified in the firmware to enable the readout of traces of arbitrary length up to the order of 1 s. Furthermore, three of them were equipped with an additional SMA input on the front panel of the digitizers' casing to receive external timing signals, such as those provided by WR.

The test system was developed in Siegen and tested in several stages on small scales (up to a few hundred meters) during the work on this project. It can be easily scaled to larger distances, for example, to the kilometer-scale separations of the detectors at Auger, by using longer optical fibers. Since WR stations can be daisy-chained, it is also possible to hook up an arbitrary number of nodes to the network, and hence an arbitrary number of stations to the test system.

This thesis begins with the discussion of the fundamental aspects of radio detection of cosmic rays, and the introduction ofthe world's largest detector array, the Pierre Auger Observatory. A description of the test system and its development is followed by an analysis of data collected using the test system at various phases of its development.

CHAPTER 2

Physics Background

2.1 Cosmic Rays

2.1.1 The Discovery of Cosmic Rays

Around the year 1900, shortly after Henri Becquerel and Marie Curie had discovered the existence of natural radioactivity during investigations of phosphorescent materials, scientists started to measure the ionization of the air. Since radioactive materials emit charged particles, it was possible to detect them through the discharge rate of electroscopes caused by the ionization of the gas inside the detector. They found that ionization was present, even in dark rooms, shielded from radioactive sources. The results in the first place were interpreted to originate from natural radioactivity, coming from the walls and the measuring device itself. To verify this assumption, in the year 1910, Theodor Wulf measured the ionization of the air at an altitude of nearly 300 m at the Eiffel Tower using a transportable electrometer. He found that the intensity of the radiation did not even decrease to half of its value compared to the level at the ground, which could not be explained by the range of α and β particles.

A few years later, in 1912, the Austrian physicist Victor Franz Hess conducted a series of measurements using hydrogen-filled balloons to measure the ionization at even larger altitudes. The crucial flight with a flight length of around 200 km took place on August 7th, 1912, where Hess went up to an altitude of 5 350 m. Figure 2.1 shows Victor Hess and his colleagues before the start of their expedition with the balloon from Aussig (today Czech Republic) to Piskow am Scharmützelsee (Germany). He found that the ionization initially decreased, as observed by Wulf during his measurements. However, after reaching a minimum at a height of approximately 1 000 m, it began to increase exponentially. In the years 1913 and 1914, Werner Kolhörster confirmed Viktor Hess' observations with a measurement of an ionization that was six times higher at an altitude of 9 km compared to the level at the surface of the Earth. Knowing now that the observed radiation has an extraterrestrial origin, Kolhörster established the name "cosmic rays". For the discovery of cosmic rays, Victor Hess received the Nobel Prize in physics in the year 1936 [1].

Figure 2.1: Victor Hess before the start of his balloon flight, where he measured the ionization of the air at an altitude of up to 5 350 m. This mounted the birth of astroparticle physics.

After its discovery, new kinds of radiation were systematically investigated, and it was found that it must consist of penetrating, charged particles. In 1938, Pierre Auger performed coincidence measurements, observing particles at a distance of 300 m from each other using two Geiger counters. With this result, he concluded that the particles detected at the surface of the Earth are not the primary particles that come from outer space, but rather are part of extensive air showers created by the interaction of a single extraterrestrial particle with the nuclei of atoms in our atmosphere. From his measurements, Auger estimated that the total number of particles in an air shower can reach one million. With the detection of energies in the GeV range, he concluded that the primary particle must have had an energy of 10^{15} eV, which was much higher than expected at that time and exceeded the energies that could be reached in experiments on Earth by many orders of magnitude.

2.1.2 The Energy Spectrum of Cosmic Rays

The energy spectrum of the primary particles spans over many orders of magnitude, reaching from MeV to more than 10^{20} eV. On October 15th, 1991, the highest energetic particle ever measured was registered in Utah at an observatory called Fly's Eye, with an energy of 3×10^{20} eV [2]. Nowadays, the spectrum of cosmic rays is well known up to the highest energies, due to a variety of experiments investigating different ranges of the spectrum via direct and indirect measurements. It has emerged that the differential flux follows, to the first order, an almost pure power law of the form

$$\frac{\mathrm{d}\Phi}{\mathrm{d}E} \propto E^{-\gamma} \tag{2.1}$$

with a spectral index of approximately $\gamma \approx 3$. In this equation, Φ denotes the particle flux, i.e. the number of particles passing through a defined area A per unit time, arriving from a specified direction Ω. The differential flux as a function of the energy is shown in Figure 2.2.

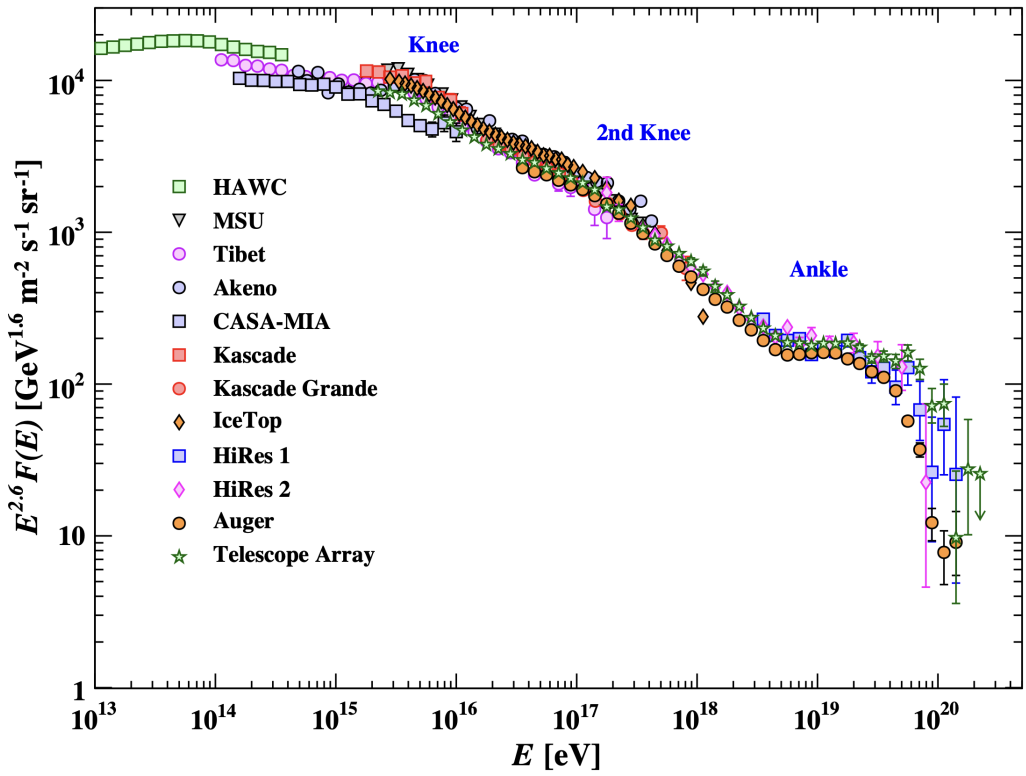

Figure 2.2: The measured energy spectrum of primary cosmic rays for all kinds of primary particles [3]. It has been measured directly for low energies and indirectly via air showers for high energies. Different measurements are marked by different colors and symbols. In order to make the changes in the spectral index more visible, the spectrum has been scaled by a factor of $E^{2.6}$.

Since the spectrum behaves like a power law with a negative index, the flux is decreasing rapidly towards the highest energies, making it extremely challenging to detect these particles with high statistical significance.

However, the spectral index is not constant, but changes from a smaller value ($\gamma \approx 2.7$) at low energies, up to 3×10^{15} eV at the *knee* of the spectrum, to a larger one ($\gamma \approx 3.0$) and back to a smaller value ($\gamma \approx 2.7$) at the *ankle*, before there is a cutoff at about 5×10^{19} eV, due to the GZK effect. At energies in the range of 10^{12} eV, a rate of a few events per second and square meter can still be measured. This value shrinks drastically to a rate approaching only approximately one event per square kilometer and year for energies above 10^{20} eV. Since the differential flux spans over multiple orders of magnitude, different parts of the spectrum must be accessed through different kinds of measurement techniques, depending on the energy range that should be investigated. Energies up to 10^{15} eV are usually measured directly, in the top layers of the atmosphere, using balloon experiments, or in space using satellite detectors like PAMELA [4], which was partially developed in Siegen to perform searches for the evidence of dark matter and to study solar modulation, in the early 2000s.

The origins of the structures in the spectrum are not fully understood and are still under investigation. A widely accepted hypothesis to explain the origin of the so-called *knee* in the cosmic ray spectrum is that it marks the upper limit of particle acceleration by astrophysical sources located within the Milky Way. This interpretation suggests that especially the light components like hydrogen and helium can only be accelerated up to a maximum energy, since the efficiency of intergalactic accelerators is limited beyond this threshold. This effect would result in a steepening of the cosmic ray spectrum.

At the ankle, located around 5×10^{18} eV, the spectrum gets flatter. It is often referred to as the transition from galactic to extragalactic sources. The spectrum of extragalactic particles is flatter than that of the Milky Way. From this point on, the previously suppressed component begins to dominate the shape of the spectrum.

There are strong hints, mainly driven by the measurements done with the SD of Auger, that there is a significant suppression of the flux at energies above approximately 3×10^{19} eV. The suppression is likely caused by the so-called GZK effect, named after the three physicists Greisen, Zatsepin, and Kuzmin, which defines a theoretical limit of the energy of cosmic ray protons [5, 6]. It is set by the interaction of protons with the cosmic microwave background (CMB), resulting in a Delta resonance that quickly decays into a proton and a neutral pion or a neutron and a positively charged pion:

$$p + \gamma_{\mathrm{CMB}} \rightarrow \Delta^{+} \rightarrow p + \pi^{0}$$

or

$$p + \gamma_{\mathrm{CMB}} \rightarrow \Delta^{+} \rightarrow n + \pi^{+}.$$

The GZK effect, hence, limits the free path of protons in the universe to a distance of approximately 100 Mpc. Above this propagation length, the energy of protons is pushed below a value of 10^{20} eV. Although there are strong indications of this effect, it has not yet been experimentally proven. A signature that would indicate the existence of the GZK cutoff

is the presence of ultra-high-energy photons, originating from the decay of neutral pions. Searches for these particles are undertaken at Auger.

2.1.3 Sources and Acceleration Mechanisms

Generally, sources of cosmic rays can be categorized into two groups. One can distinguish between galactic sources and extragalactic sources. Which of the two classes is more dominant will depend on the energy range. Whereas cosmic rays up to the knee at 3×10^{15} eV are assumed to be originating from galactic sources, energies above the ankle are assumed to have an extragalactic origin. At the lowest energies in the MeV to GeV range, the Sun is typically considered as the primary source of cosmic rays. Sunspots can produce intense starbursts while coronal mass ejections produce low-energy particles. During solar flares, charged particles are released and can be accelerated through Sun's magnetic field. Possible candidates for galactic sources of more energetic cosmic rays than those produced by the Sun are supernova remnants (SNRs) or pulsars, i.e. rapidly rotating neutron stars with magnetic fields up to 10^8 T [7] from which SNRs are the most dominant ones. Extragalactic sources, on the other hand, can be active galactic nuclei (AGNs), gamma-ray bursts (GRBs) or starburst galaxies. An AGN is the center of a galaxy where the density of material is maximal and new stars are created abundantly. GBRs are short and bright flashes of gamma rays, originating from the fusion of two compact objects like neutron stars or the supernova of a heavy star with a mass $M > 25M_{\odot}$.

Two mechanisms for the acceleration of charged particles in the cosmos have been proposed by Enrico Fermi. As a thermal origin has been excluded because the spectrum of cosmic rays shows the behavior of a power law, Fermi first proposed a stochastic acceleration in turbulent magnetic fields. According to this approach, charged particles gain energy in head-on collisions with a plasma cloud in the interstellar medium. This process is called *second-order Fermi acceleration* as the energy gain per collision scales with the square of the velocity of the plasma cloud. However, it turned out that this process is too slow to explain energies above PeV range.

A second mechanism to describe the acceleration of cosmic rays is the shock acceleration, or *first-order Fermi acceleration*. Here, particles gain energy by crossing the shock front of a supernova. Every time particles cross the shock front, they gain a fractional energy proportional to the velocity of the shock front. If a particle remains in the shock region, it can encounter multiple head-on collisions, leading to a rapid acceleration. However, after each collision, there is also a possibility for the particle to leave the shock front and hence no longer be accelerated.

Both processes naturally produce power-law spectra, which is consistent with the observations of the cosmic ray spectrum. The total energy gain, in either case, depends on the number of collisions with the plasma or the shock front, respectively. As the energy the particles gain increases, they are more likely to escape the region of acceleration, since the particles have to be trapped magnetically. The maximum energy a particle can reach is proportional to the size

of the object, its magnetic field, and its velocity:

$$E_{\max} \propto Z \cdot R \cdot B \cdot \beta. \tag{2.2}$$

As the maximum energy scales with the charge of the particle Z, heavier nuclei can therefore be accelerated to proportionally higher energies. According to this formula, supernovae can produce cosmic rays up to an energy of

$$E_{\max} \approx Z \cdot 10^{15}\,\text{eV}, \tag{2.3}$$

which confirms them to be a likely candidate for galactic sources. Considering the size and magnetic field strength of different astrophysical objects, one can estimate the maximum achievable energy from several potential sources. These objects can be classified in the so-called Hillas plot, which is shown in Figure 2.3, where they are sorted according to their magnetic field strength and size. However, it turns out that only a minority of the sources can produce protons with an energy above 10^{20} eV, leaving the sources for the highest energies still unrevealed. In addition, intergalactic magnetic fields, which are only known to a limited extent, deflect charged particles from their straight path, making it hardly possible to trace them back to their origin.

2.2 Extensive Air Showers

When the highly energetic primary particles from outer space reach the Earth, they interact with the nuclei of the atoms that form the molecules of the atmosphere. In most cases, this is a nitrogen or oxygen nucleus according to the composition of the air. Depending on the energy of the primary particle, a large amount of secondary hadrons like pions and kaons, but also other baryons, are produced and propagate through the atmosphere and interact again with other nuclei. This cycle of propagation and interaction can happen multiple times. In each interaction, the secondary particles lose a part of their energy by transferring it to the partner of the interaction. At the same time, the number of particles in the shower increases exponentially until an atmospheric depth is reached where the number of particles is maximal. This is called the shower maximum, usually referred to as $X_{\max}$, and it is an important parameter of an air shower, as it can be used to reconstruct the identity of the particle that initiated the cascade in the air. Typically, in the context of cosmic ray air showers, X is referred to as the atmospheric depth. It is a measure of the amount of material particles passing through and, therefore, another value to describe the distance the shower travelled through the atmosphere. The atmospheric depth is calculated from the density ρ of the atmosphere, which is not constant but decreases with increasing altitude. If one considers ρ to be a function of the altitude $\rho(z)$, the atmospheric depth is calculated via the following integral:

$$X(h) = \int_h^\infty \rho(z)\mathrm{d}z. \tag{2.4}$$

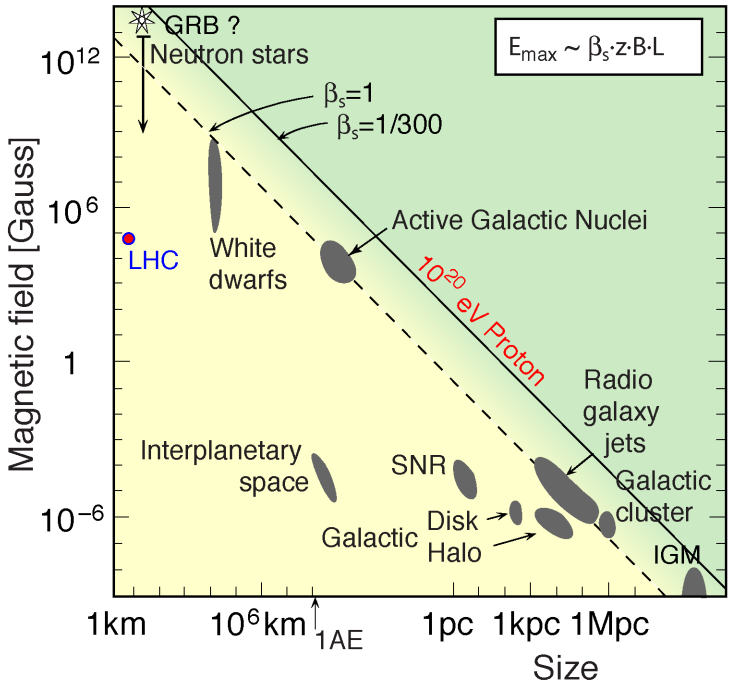

Figure 2.3: The Hillas plot, originally from [8], relates the size of potential astrophysical sources for cosmic rays to their magnetic field. The diagonal lines indicate a threshold in size and magnetic field strength above which cosmic rays with energies above 10^{20} eV can be produced. The solid line represents the threshold for a proton and the dashed one for an iron nucleus. The threshold is defined by the criterion that particles have to be magnetically trapped in the astrophysical object.

In a simple model, $\rho(z)$ can be described by an exponential decrease

$$\rho(z) = \rho_0 \exp(-z/z_0), \tag{2.5}$$

where ρ_0 is the density of the air at sea level. However, in reality, things are more complicated, as the temperature of the atmosphere is not constant with altitude, and weather phenomena can alter the density locally. A good estimate for the atmospheric depth at the surface of the Earth is $1\,030\,\mathrm{g\,cm^{-2}}$ [9].

The further the shower penetrates the atmosphere, the less energy each individual particle carries, and the number of particles starts to decrease again until the shower finally dies out. Since there are thresholds for specific processes (e^+e^- production works only above an energy threshold of $2m_e \approx 1.022\,\mathrm{MeV}$) and energy losses which limit the range of particles in a medium like air, not all particles can reach the surface of the Earth, but are absorbed on their way towards the ground. This effect gives the shower a characteristic longitudinal profile.

As can be seen in Figure 2.4, not every particle creates the same shower profile. The maximum number of particles in the shower depends on the energy of the primary particle as well as on the type of particle. Thus, for example, $X_{\max}$ for a proton-induced air shower is typically around 800 g cm^{-2} while that of an air shower generated by an iron nucleus with the same primary energy is in the range of 700 g cm^{-2}. This means that there is a difference of roughly 100 g cm^{-2}, which offers the possibility to distinguish the two types of particles. However, it is not guaranteed that all proton showers have a smaller $X_{\max}$ than iron showers. As the diagram also shows, there are large fluctuations in the depth of the shower maximum, especially for the proton-induced showers, which makes an event-by-event classification much more difficult. Statistical methods like Monte-Carlo simulations are necessary to distinguish, for example, a primary proton from iron by the fluctuation of $X_{\max}$. For example, iron showers have a smaller fluctuation than proton showers. Photon showers, on the other hand, tend to penetrate deeper into the atmosphere and hence have a large $X_{\max}$, which unfortunately also comes with greater uncertainty.

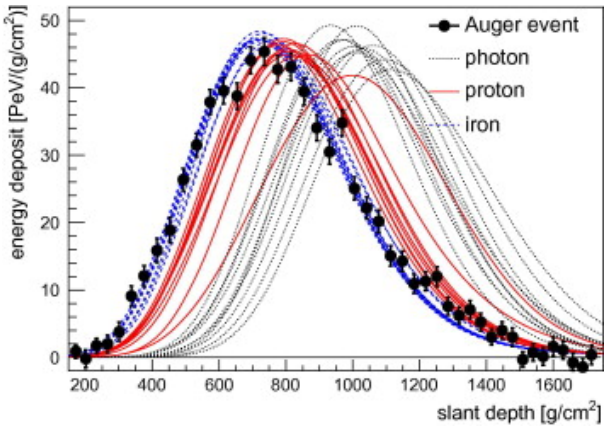

Figure 2.4: An example for a longitudinal shower profile from [10]. The black markers show the data points measured at Auger. The measurements are compared to simulated air shower events created by a photon (grey), a proton (red) or an iron nucleus (blue).

Similary to the protons and other nuclei that reach the Earth, the secondary particles are also highly relativistic and hence moving close to the speed of light. This leads to an almost flat, disk-shaped shower front which, depending on the energy of the primary particle, can reach a size of a few square kilometers while the thickness of the disk is in the order of meters. The direction in which the disk is moving is called the shower axis. Most of the particles, especially the hadrons, are concentrated at the center of this disc. The total number of secondary particles, dominated by the electromagnetic cascade, can be approximated by

$$N_{\text{tot}} \approx E_0/\text{GeV} \tag{2.6}$$

where E_0 is the energy of the primary particle that hits the atmosphere. This means that a

shower, initiated by a 10^{18} eV proton, contains a total number of around one billion secondary particles.

An extensive air shower can be divided into three main components:

- a hadronic component,
- a muonic component and
- an electromagnetic component.

The hadronic component forms the backbone of the air shower, supplying charged and neutral pions that act as initiators for the muonic component in case of the charged pions and for electromagnetic cascades in case of neutral pions. The development of a typical air shower is depicted in Figure 2.5. The three individual components will be discussed in the following. Particular attention is paid to the electromagnetic component as it is responsible for radio emissions, which play a crucial role in the work of this thesis.

2.2.1 Electromagnetic Component

The electromagnetic component of an air shower is created by the decay of neutral pions. With an average lifetime of 8.5×10^{-17} s, it decays via an electromagnetic interaction, explaining the short lifetime compared to charged pions, which only decay via weak interaction. The most dominant decay mode is the one where the pion goes into two photons:

$$\pi^0 \rightarrow \gamma\gamma. \tag{2.7}$$

This process has a branching ratio of 98.823% and thus nearly all high-energy neutral pions will initiate an electromagnetic shower. The further interactions can be, in good approximation, described by the model of an electromagnetic cascade, presented by Heitler, which was able to extract critical physical relations between the energy of the leading particle and observables like the total number of particles in the cascade and the depth of the shower maximum. Figure 2.6 depicts a schematic view of an electromagnetic cascade. However, it is essential to note that this model describes a very simple conception of electromagnetic showers and does not accurately capture all interactions, such as those that occur in a real cascade.

The Heitler model assumes that after passing a mean distance $X_0 = \lambda_{\text{rad}} \ln 2$ through the atmosphere, the photon interacts in the presence of the electric field of a nucleus from an air molecule and splits into a pair of an electron and a positron. Here, λ_{rad} is the radiation length, which is a characteristic property for a given material, describing the mean free path of electrons in this medium. After traveling this distance, the electron has in average lost half of its energy through the emission of bremsstrahlung. In the case of photons, this value can also be used to describe the average distance photons travel in a medium before they form a pair of electron and positron.

In air, the standard value for the mean free path is given by $\lambda_{\text{rad}} = 37.15\,\text{g}\,\text{cm}^{-2}$ and can be found in [12]. Each of the new particles, the electron and the positron, will, according to the assumption in Heitler's model, carry half of the energy of the original photon. After passing

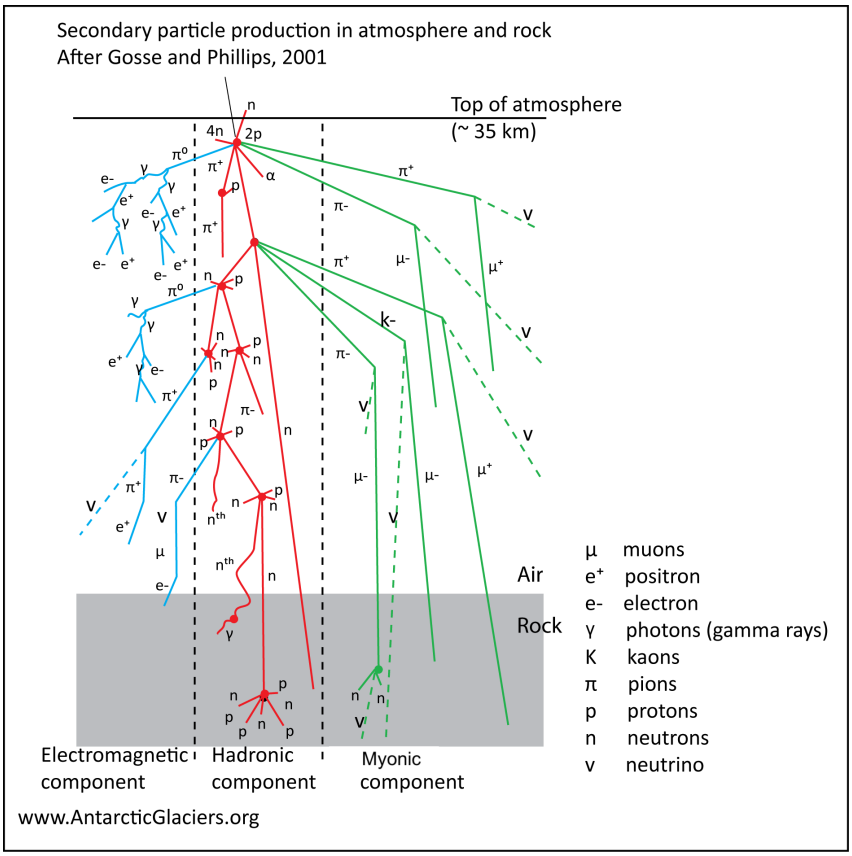

Figure 2.5: An illustration of the development of a cosmic ray-induced air shower, adapted from [11]. The shower is split into three components: an electromagnetic component (blue), a hadronic component (red) and a muonic component (green).

another mean distance X_0, the two particles will emit two new photons via bremsstrahlung. The processes of pair production and bremsstrahlung will be repeated alternately, one after the other. In each step, the number of particles doubles, while the energy of the individual particles is halved. It therefore follows that the number of particles in the electromagnetic shower increases exponentially with the number of interactions that happen and after traversing a distance $D = n \cdot X_0$ in the atmosphere, the cascade consists of a total number of

$$N_n = 2^n \tag{2.8}$$

particles with equally distributed energy, such that each particle carries a fraction of

$$E_n = \frac{E_0}{2^n}, \tag{2.9}$$

where E_0 is the energy of the primary particle.

Since cosmic rays that create air showers are in the ultra-high energy regime, it is valid to assume that other interactions between photons and electrons, like Compton scattering and the photoelectric effect, can be neglected due to the strongly suppressed cross-section. Above energies of 100 MeV, pair production becomes the most dominant process. Conversely, however, this also means that the electromagnetic cascade does not continue forever. Since the energy of the particles decreases with each step, one can define a critical energy E_{crit} which indicates the threshold to keep the cascade alive. If the energy drops below this critical value, pair production and bremsstrahlung are no longer the dominant interactions. Instead, the particles in the shower will mainly lose their energy by ionization through scattering processes with air molecules. As the interactions are also a statistical process, and we defined mean values for the free path length, not all particles will fall below the threshold at the same time. In reality, it is more of a slow extinction of the shower. However, as it can also be seen in Figure 2.4, there is a point where the number of particles in the shower reaches a maximum value when the energy of a single particle is equal to

$$E_{\text{crit}} = \frac{E_0}{2^{n_{\text{max}}}}. \tag{2.10}$$

This equation can be rearranged to get the number of interactions that have happened before the maximum:

$$n_{\text{max}} = \frac{\ln\left(\frac{E_0}{E_{\text{crit}}}\right)}{\ln 2}. \tag{2.11}$$

At this point, there are

$$N = 2^{n_{\text{max}}} = \frac{E_0}{E_{\text{crit}}} \tag{2.12}$$

particles in the shower. As one interaction in average corresponds to an atmospheric depth of X_0, one can calculate the position of the shower maximum by

$$X_{\text{max}} = X_0 \cdot n_{\text{max}} = X_0 \cdot \frac{\ln\left(\frac{E_0}{E_{\text{crit}}}\right)}{\ln 2}. \tag{2.13}$$

Although the model is relatively simple, it reveals two important properties of air showers. On the one hand, the number of particles at the shower maximum is proportional to the total energy of the primary particle E_0, while on the other hand, the position of the shower maximum X_{max} scales with the logarithm of the energy. However, it should be mentioned that if the air shower was induced by a hadron and hence contains a hadronic component, there is not only a single electromagnetic cascade, but rather a superposition of many electromagnetic cascades formed during the hadron multiplication in the atmosphere. Due to their, compared to hadronic interactions, short free path length, electromagnetic cascades usually die out in the upper atmosphere before they can reach the ground. But if the primary particle was a high-energy electron or photon, it is indeed possible to create a purely electromagnetic shower, which in exceptional cases can reach the surface of the Earth and be directly detected.

Even if the cascade does not reach the ground, it is still possible to gain information about the development of the electromagnetic shower by applying complementary measuring principles. As the content of the air shower being detected at ground level is a mixture of different particles, one has to separate the electromagnetic component with dedicated analysis methods. As we will see later, electrons and positrons emit radio signals that an array of radio antennas on the ground can detect. This method provides dedicated insights into the electromagnetic component of the air shower.

2.2.2 Hadronic Component

The hadronic component of an air shower is primarily caused by a hadron–hadron interaction between the primary cosmic particle (in this case, a proton or a nucleus) and an air nucleus (mostly nitrogen or oxygen). During this interaction, mostly pions and kaons are produced. As shown in [13], it is also valid to assume a Heitler cascade for the hadronic part of an air shower. For simplification reasons, kaons will be neglected in the following considerations. While the neutral pions decay immediately after formation (see above), charged pions can, depending on their energy, perform further hadronic interactions before they finally decay into muons. According to this model, $1/3$ of the hadrons created after traversing an average distance of $\lambda_{\text{had}} \cdot \ln(2)$ where in this case, λ_{had} is the hadronic interaction length, are neutral pions, while $2/3$ are charged. Consequently, and in contrast to the electromagnetic shower, the hadronic shower loses $1/3$ of its energy via interaction. Therefore, the mean energy per charged pion after n interactions is given by

$$E_\pi^\pm = \frac{E_0}{\left(\frac{3}{2}N_{\text{ch}}\right)^n}, \tag{2.14}$$

where N_{ch} is the average multiplicity of charged particles in hadronic interactions. As one hadron can produce several new hadrons in a collision, this number does not have to be constant, whereas in an electromagnetic cascade, the multiplicity is always two (see above). The evolution of a hadronic cascade is shown in Figure 2.5 in the right panel. Analogously to the electromagnetic shower, a critical energy can also be defined for pions. The production of further pions stops if the energy of the mesons falls below a threshold E_{crit}^π. According to [13], this value can be estimated by the energy where the decay length $\gamma\beta ct$ drops below the average distance between two interaction points, calculated using the hadronic interaction length λ_{had} and the density profile of the atmosphere. However, it can be shown that this value is not constant but decreases as the primary energy increases. The critical energy for a proton-induced hadronic shower has been estimated to be $E_{\text{crit}}^\pi = 30\,\text{GeV}$ for $E_0 = 100\,\text{TeV}$ and $E_{\text{crit}}^\pi = 10\,\text{GeV}$ for $E_0 = 100\,\text{EeV}$, which indicates that E_{crit}^π slowly decreases with increasing energy of the primary proton.

Besides the simplified assumptions like a constant λ_{had} over a wide range of energies and a constant value of the particle multiplicity in each interaction, modelling hadronic interactions always comes with larger uncertainties than electromagnetic models. Therefore, they are the

main source of uncertainties in the determination of the primary particle. The reason for this is the absence of experimental data for hadronic interactions at ultra-high energies like the ones in cosmic ray-induced air showers. Furthermore, the strong interaction is generally less well-known than the electromagnetic interaction, leading to less precise predictions of the shower development.

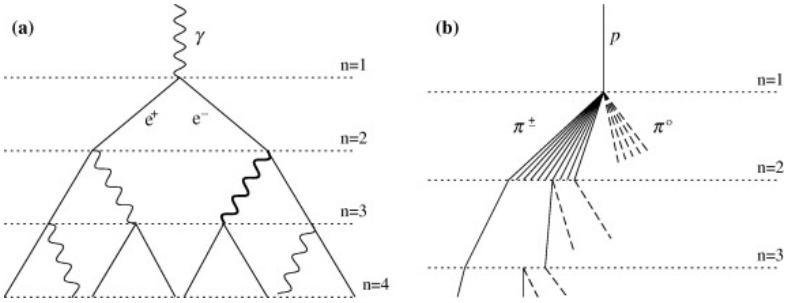

Figure 2.6: Left: A schematic view of an electromagnetic cascade started by a single photon. The number of particles doubles at each interaction, which is indicated by horizontal lines. Photons are radiated and produce a new e^+e^- pair after passing a distance of one radiation length in air. Right: A proton collides with a nucleus in the atmosphere, where a bunch of charged and neutral pions are produced. Charged pions will interact again after passing one hadronic interaction length, while neutral pions decay into photons, contributing to the electromagnetic cascade. Illustration is taken from [13].

2.2.3 Muonic Component

The muonic component plays an important role in the detection of air showers on ground level, as it provides information about the hadronic component. Muons are mostly produced in the upper atmosphere at an altitude of about 15 km above sea level. They are created almost exclusively through the decay of unstable and therefore short-lived charged pions and kaons

$$\pi^{\pm} \rightarrow \mu^{\pm} + \nu_{\mu}$$
$$K^{\pm} \rightarrow \mu^{\pm} + \nu_{\mu}$$

originating from the hadronic cascade. The number of muons produced at a given stage of the cascade depends on the altitude of the hadronic shower. Since the atmosphere is less dense at large altitudes, hadrons can travel larger distances before they interact with an air molecule, and hence the probability for the pion to decay is larger than close to the ground, where pions and kaons interact more likely with the atmosphere. One can therefore say that air showers traversing the atmosphere at a large zenith angle produce more muons, because the mesons travel at a larger altitude for a longer time and therefore more likely to decay.

Once a muon is created, it can travel almost undisturbed through the atmosphere due to its high penetration capability. Because the energy loss due to bremsstrahlung scales with the

inverse of the square of the mass of the particle, muons, in contrast to electrons, radiate only a negligible amount of their kinetic energy. Furthermore, since muons are leptons, they do not interact via the strong force, making it unlikely for them to interact with nuclei or other hadrons.

Compared to other particles, muons are rather long-lived and have a lifetime of $\tau = 2.2\,\mu s$ before they decay into an electron and two corresponding neutrinos via

$$\mu^{\pm} \rightarrow e^{\pm} + \nu_e + \nu_\mu$$

with a branching ratio close to 100%. However, due to relativistic time dilation, a considerable proportion of the muons manage to reach the ground and are used to detect the air shower. The distance d a muon can travel if not interacting, which is unlikely due to its low interaction probability as described above, can be calculated from

$$d = \gamma\beta ct. \tag{2.15}$$

Thus, a muon with an energy of 2 GeV can travel a distance of approximately 12 km and therefore has a good chance of reaching the ground and being registered by a surface detector. But not all muons have such a high energy, and some of them will decay on their way downwards. The electrons produced in this process can then contribute to the electromagnetic cascade.

In the decay of a muon, not only is an electron produced, but also two neutrinos. These can also propagate undisturbed, but don't play a significant role in air shower measurements, as it is nearly impossible to detect them because of their small cross-section. On the other hand, dedicated experiments are searching for high-energy neutrinos, where these so-called atmospheric neutrinos are treated as background.

2.3 Radio Emission of Extensive Air Showers

Alongside the particle detection on ground level and the production of fluorescence light from excited nitrogen atoms in the atmosphere, air showers are also producing electromagnetic radiation in the radio regime, which has been successfully observed between 2 MHz and 500 MHz [14]. The radio waves are created through the collective movement of electrons and positrons in the electromagnetic component of the shower, as they are easy to accelerate because of their low mass. The dominating processes are two macroscopic mechanisms: The geomagnetic effect, which is based on the deflection of electrons and positrons in Earth's magnetic field, and the Askaryan, or charge excess, effect, which results from a time-varying imbalance between positive and negative charge carriers. Both mechanisms create short, coherent radio pulses that overlap, and their properties allow conclusions to be drawn about the development of the air showers.

2.3.1 Geomagnetic Deflection

When the charged particles are passing through the atmosphere, they are accelerated by the Lorentz force

$$\vec{F} = q\vec{v} \times \vec{B}, \tag{2.16}$$

which acts perpendicularly to the geomagnetic field $\vec{B}$ and their direction of propagation $\vec{v}$. Since electrons and positrons are oppositely charged, they will be deflected in different directions. While the magnetic force deflects the particles, they lose a part of their energy as a result of frequent random scattering processes with air molecules. In the reference frame of the shower, this results in a state of equilibrium where the collective movement of charge carriers can be treated as a transverse current $\vec{J}_\perp$. This phenomenon can be seen in analogy to the movement of electrons in copper, with the difference that the electrons (and positrons) in this case are not moved by an external voltage but by Earth's magnetic field. Since the shower develops and the number of charge carriers increases, reaching a maximum and then decreases when the shower dies out, this current is time-dependent, reaching a maximum coinciding with the shower maximum $X_{\max}$. According to electrodynamics, this results in the emission of electromagnetic waves where the amplitude

$$\vec{E}_{\text{geo}} \propto \frac{\mathrm{d}\vec{J}_\perp}{\mathrm{d}t} \tag{2.17}$$

of the electric field is proportional to the variation of the current. Therefore, it approximately scales with the number of particles $N(t)$ and hence with the energy of the primary particle. The polarization of the radio signal is linear and, in this case, aligned with the $\vec{v} \times \vec{B}$ axis and is independent of the position of the observer.

The presence of the geomagnetic effect also depends on the geomagnetic angle α, i.e. the angle between the direction of propagation and the magnetic field, and is proportional to $\sin\alpha$. Suppose the shower is moving in parallel to the alignment of the Earth's magnetic field. In that case, the emission vanishes because there is no Lorentz force acting on the electrons, while it becomes maximal for particles moving perpendicularly to it, where $\sin\alpha = 1$. This type of emission has been proposed by Kahn and Lerche in 1966 [15]. A macroscopic model to describe the coherent electromagnetic radiation from air showers has been developed in [16]. The model describes the relation between properties of the air shower and the structure of the radio pulse that can be measured using radio receivers. A graphical representation of the effect and the polarization of the resulting radiation can be found in Figure 2.7. The polarization is shown in the shower plane, which is perpendicular to the shower axis and spanned by the $\vec{v} \times \vec{B}$ and the $\vec{v} \times \vec{v} \times \vec{B}$ axis.

2.3.2 Charge Excess

During the evolution of the air shower, a negative charge excess is created in the shower front. Two reinforcing effects play a decisive role here. As the atoms in the air get hit by the particles from the shower, they can be ionized and hence produce free electrons. Additionally, further free electrons can be generated by Compton scattering. These extra electrons will

move along with the shower front while the much heavier positive ions remain behind due to their inertia. Meanwhile, positrons can also interact with the surrounding material and annihilate randomly with an electron from an atom, resulting in a reduction of the number of positive charge carriers. In sum, this results in a total charge excess of approximately 10% to 20% near $X_{\max}$. Similar to the geomagnetic effect, the charge excess is also not constant. The amount of negative charge carriers present in the shower increases with an increasing total number of particles, as more electrons in the shower can ionize a larger number of atoms. The resulting charge excess is therefore also time-dependent and leads to a pulse of electromagnetic radiation. In addition, electrons in the air shower moving close to the speed of light can also produce a Cherenkov-like emission, contributing to the total amount of radio signals. Its polarization, unlike the one from radiation caused by the geomagnetic effect, depends on the position of the observer, since the electric field is oriented radially with respect to the shower axis. The charge excess effect is also called the Askaryan effect, named after its discoverer in 1961 [17]. A graphical representation of the effect and the polarization of the resulting radiation is shown in Figure 2.7.

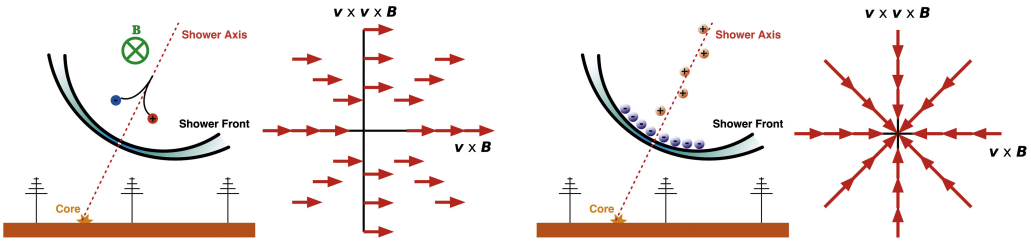

Figure 2.7: Left: A graphical representation of the geomagnetic mechanisms. Opposite-sign charges are separated through the geomagnetic field. The resulting polarization is indicated by the red arrows, pointing in the direction of the Lorentz force ($\vec{v} \times \vec{B}$). Right: A graphical representation of the Askaryan effect. An excess of negatively charged particles is accumulated in the shower front. Red arrows indicate the radial polarization of the radiation. The radiation is polarized in the plane perpendicular to the shower axis. The diagrams are originally from [18] and [16] and adapted in [14].

2.3.3 Superposition and Observable Signatures

In general, the radiation due to charge excess is small compared to the geomagnetic deflection and contributes only 10% to the total amplitude of the electric field [19]. However, as the radiated waves from both processes will interfere, it is only possible to observe their superposition of the electric fields. Due to different polarizations, the sum of the electric field results in an asymmetry of the radio footprint observable on the ground, because the two contributions can overlap either constructively or destructively. An example of the geometry of a radio signal on the ground can be found in Figure 2.8. Besides that, the asymmetry also changes with the direction of the shower axis, as the relative share of the geomagnetic radiation depends on the angle between the shower axis and the local magnetic field of the Earth.

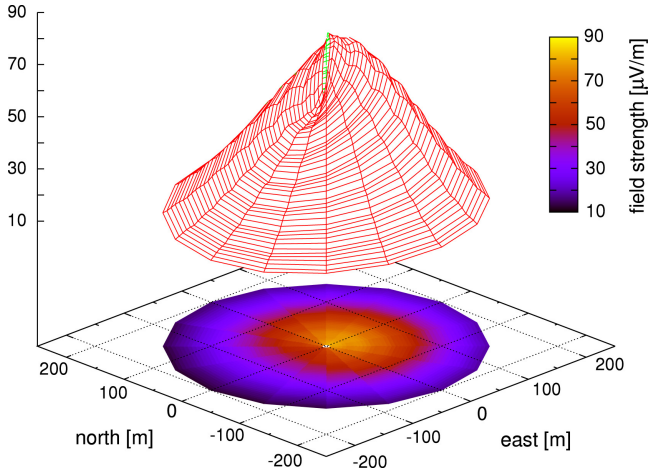

Figure 2.8: A simulation of the electric field on the ground, caused by a vertical cosmic ray air shower induced by a 10^{17} eV iron nucleus [14]. The east-west asymmetry is coming from the combination of the geomagnetic and charge excess emissions.

A crucial aspect of the radio signals emitted by air showers is their coherence. Multiple small emissions have the same phase, so that their signals will add up constructively, resulting in a linear increase of the radiated field strength with the number of emitting particles N. Therefore, the power emitted by the radiation of an air shower scales quadratically with N and hence also with the energy of the primary particle, as it has been shown in Equation (2.12). With incoherent emission, on the other hand, only the intensities add up, and the strength increases with $\sqrt{N}$.

In the shower front, several hundred million charged particles are moving together, all of them with almost the same velocity, namely the speed of light. These particles are all propagating in the same direction, concentrated in a thin disk compared to its expansion (which is sometimes called *pancake* due to its flat shape) with a thickness of only a few meters. As long as the thickness of the disk is small compared to the radiated wavelength, the signals are usually in phase and hence coherent. However, as the frequency increases and the wavelength drops below the thickness of the *pancake*, which is typically above a frequency of 100 MHz where $\lambda = 1$ m, phase differences have a more substantial influence and will cause destructive interference, resulting in the loss of coherent behavior.

Because of the relativistic speed of the particles, the radiation is strongly focused in the forward direction, creating a cone-shaped structure with a few degrees opening angle and a radius of around 100 m to 200 m on the ground. In addition, the refractive index of the air is not constant, but increases exponentially with decreasing altitude as the air gets denser towards the sea level. Therefore, the velocity of electromagnetic waves in the atmosphere depends on the altitude, and it is faster in the upper atmosphere than near the ground. The signals created at different altitudes arrive as a compressed pulse in a ring-shaped structure called the Cherenkov Ring. The received pulse has a bipolar shape and its length is in the

order of a few nanoseconds. An example for such a pulsed radio signal can be found in Figure 2.9, where the time characteristic of the signal shape has been simulated for different parametrizations of the refractive index. At this point, it is essential to note that a clean pulse shape like the one shown in the simulation cannot be observed in experimental data. As we will see later, the antenna response and the electronics in the data acquisition system have a strong influence. They will deform and stretch the shape of the pulse due to their bandpass characteristics.

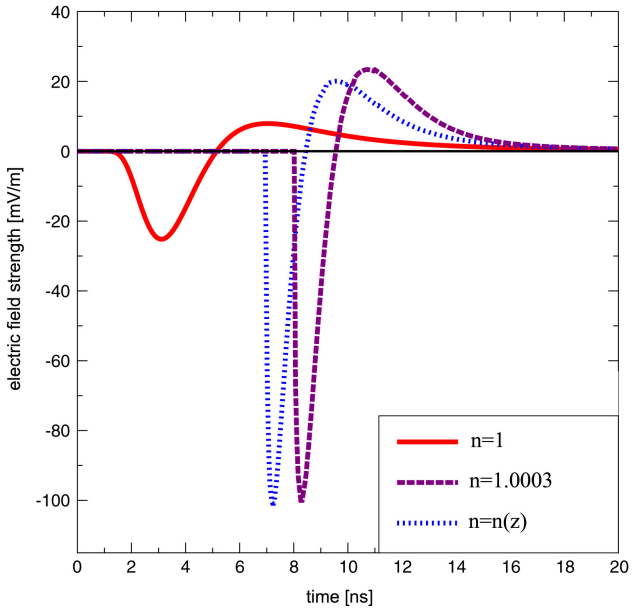

Figure 2.9: A typical radio pulse simulated for a 5×10^{17} eV cosmic ray particle [20]. The different curves indicate different models for the refractive index resulting in different shapes and different times of arrival.

Even though the radio emissions are strongly boosted in the forward direction, the location of the source affects the shape of the footprint that can be measured on the ground. If the emission is happening at higher altitudes, the pulses travel a longer geometric distance. As a result, the cone will have a larger radius and thus illuminate a larger area. Something similar happens when the air shower does not pass through the atmosphere vertically, but comes in at an angle θ. This kind of air shower is called *inclined*. The distance travelled in the atmosphere scales with $1/\cos(\theta)$ and increases with θ. Therefore, more inclined air showers reach their X_{max} further up, which leads to an increased distance between the shower maximum and the observer. Similarly, the illuminated area is larger. As a consequence, the amplitude of the electric field in each detector station is lower because the radiated power depends primarily on the energy of the cosmic ray. The signal-to-noise ratio decreases, which makes the reconstruction of the shower properties less precise.

2.4 Radio Interferometry

Interferometric techniques are employed in various fields of physics. They are widely used in radio astronomy, where supernova remnants, pulsars, or even whole galaxies are studied using large-scale radio telescopes. This idea has recently been adopted to apply interferometric measurements also to the coherent radio emissions of cosmic ray-induced air showers. The idea is based on the fact that a detector array can act as an interferometer, as multiple antennas measure the electric fields induced by the same source. If the recorded traces can be aligned with high precision, features of the air shower signal can be enhanced while noise contributions are suppressed. These features can be further used to reconstruct the origin of the emission, and hence the depth of the shower maximum $X_{\max}$, with higher precision than classical methods based on the time of arrival. A method to extract this information has been developed in [21], which serves as a reference for the following section. Here, the waveforms $S_i(\vec{x}, t)$ recorded by the array of antennas at different locations a_i are summed up while taking into account the different propagation times for the signal. This results in a total amplitude given by

$$S(\vec{x}, t) = \sum_{i=1}^{n} S_i\left(t + \Delta_i(\vec{x})\right), \tag{2.18}$$

where $\Delta_i(\vec{x})$ is the propagation time from the position of the source $\vec{x}$ to the location of the antenna i. The propagation time depends not only on the geometric distance, but also has to take into account the refractive index of the air. In the approach in [21], the average refractive index, parametrized by an exponential function and increasing with decreasing altitude, along the straight path from the source to the receiver, has been used to calculate the transit time of the signal with the formula

$$\Delta_i(\vec{x}) = \frac{|\vec{x} - \vec{a}_i|}{c} \overline{n}_i. \tag{2.19}$$

In contrast to classical radio interferometry, where the studied objects are far away and can be assumed to be point sources, the emission occurs much closer to the receivers, and the source has a non-negligible spatial extent. Therefore, the time delays between a location $\vec{x}$ and an antenna $\vec{a}$ have to be calculated individually for each $\vec{x}$. Figures 2.10 and 2.12 show the distances from a source at a location $\vec{x}$ to an array of four antennas on the ground, located at positions $\vec{a}_i$, with signal propagation times Δ_i. The true position of the source is indicated by the black dot at S_0. Different colors mark the paths to different antennas. In Figures 2.11 and 2.13, the individual signals, recorded by antennas at different locations, as well as the sum calculated according to Equation 2.18, are shown. The individual signals have colors corresponding to the path that has been taken to calculate their delay. The sum of all signals is shown as a dashed, grey line.

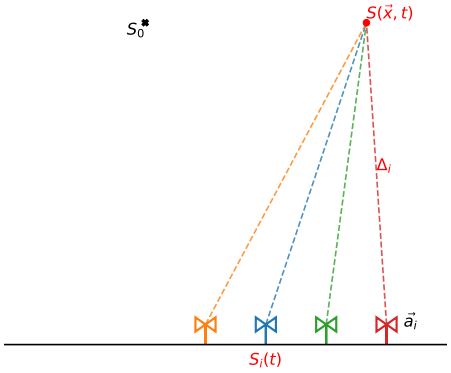

Figure 2.10: Source mapping using radio interferometry. S_0 marks the true source. Each antenna and the path to the reconstructed source are indicated by a specific color. The geometrical distance Δ_i to the reconstructed source at $S(\vec{x}, t)$ is far from the true source.

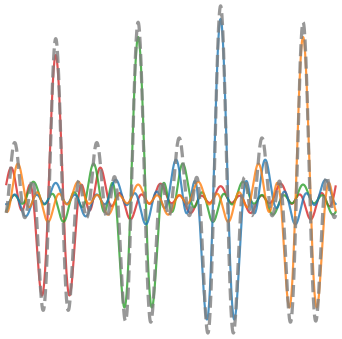

Figure 2.11: An overlay of traces from a wrongly located source. The colors correspond to the antennas in the adjacent illustration. The sum of all antenna traces is shown by the grey curve. The distance to the true source results in a sum where no clear features of the signal are visible.

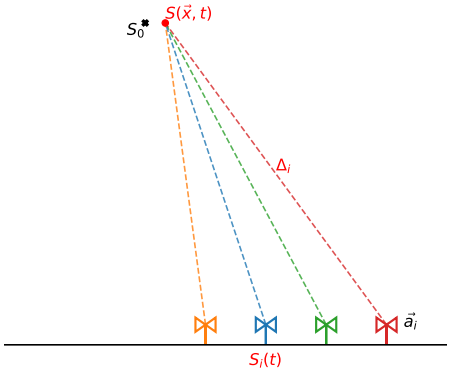

Figure 2.12: Source mapping using radio interferometry. S_0 marks the true source. The geometrical distance Δ_i to the reconstructed source at $S(\vec{x}, t)$ is close to the distance to the true source.

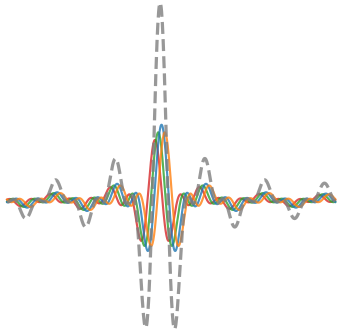

Figure 2.13: An overlay of traces where the located source is close to the true source. In the sum of the individual traces (grey curve), the signal is enhanced and better visible. This enables the extraction of physical parameters.

As can be seen in Figure 2.11, the shape of the summed signals does not enhance the features (pulses) of the individual signals, making it hard to extract any information from this data because the signal-to-noise ratio does not improve. However, when the location where the source is assumed to be gets closer to the actual source, the traces start to align better, resulting in an amplified signal increasing with the number of receivers. In contrast, noise is still adding incoherently and is therefore growing more slowly than the signal. This behavior can be seen in Figure 2.13, where the grey curve has an amplitude more than twice that of a single antenna. At this point, the signal-to-noise ratio improves significantly, resulting in a more precise reconstruction of the physical parameters.

In order to reconstruct the shower axis, the emitted power, which is proportional to the square of the electric field strength, can be calculated for a discrete set of locations $\vec{x}$. This creates a three-dimensional power distribution, which shows a strong correlation with the direction in which the air shower is traveling. At an altitude where the shower maximum is assumed based on simulations, a horizontal plane is defined, and the position of maximum power emission is determined iteratively to get a position that is assumed to lie on the shower axis. This process is repeated for different horizontal planes, which results in a set of maxima. Afterwards, a linear fit is performed to obtain the parameters of the shower axis. Finally, with these parameters, the power emitted along the axis is calculated, and the position of the maximum is searched. An example of such a power mapping is shown in Figure 2.14, where the vertical development as well as three horizontal slices can be seen. In panel *c*), the altitude is close to the position of X_{max} and hence the emission is the strongest.

Using air shower simulations, it has been shown that the depth of the maximum of the radio emissions depends linearly on the position of the shower maximum X_{max} and hence can be reconstructed from the maximum of the power distribution. The resolution of X_{max}, on the other hand, is strongly influenced by the receiver-to-receiver time synchronization, as it can be seen in Figure 2.15. It improves by roughly a factor of two going from 4 ns timing down to 2 ns and can drop below $10\,\mathrm{g\,cm^{-2}}$ for a synchronization below 1 ns. This would improve the resolution of X_{max} by a factor two compared to current methods applied to the measurements with fluorescence telescopes at Auger, where the resolution varies between $25\,\mathrm{g\,cm^{-2}}$ at an energy of 10^{18} eV and $15\,\mathrm{g\,cm^{-2}}$ at an energy of 2×10^{19} eV or larger [22]. In addition, radio interferometry could be combined with other techniques to get a more detailed insight into the primary cosmic particle. To reveal the full potential of this technique, it is necessary to ensure sub-ns time synchronization on large-scale detector arrays like Auger, where antennas are spaced at a distance of up to 1.5 km. This task remains challenging due to the absence of a common, wired clock, GPS drifts, or changing environmental conditions in the detector area.

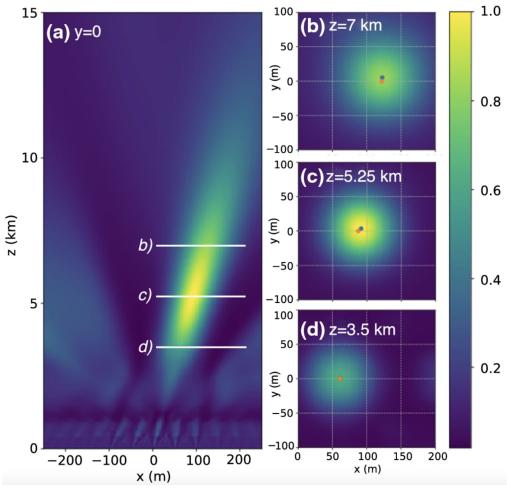

Figure 2.14: Simulations of the reconstructed power calculated in radio interferometric analysis [21]. The power is normalized such that the maximum is equal to 1. Panel *a*) shows the vertical distribution of the power projected onto the $y = 0$ plane. Three horizontal planes at different altitudes are shown in panels *b*), *c*) and *d*). The orange dots show the true shower axis, and the blue ones indicate the point of maximum power emission.

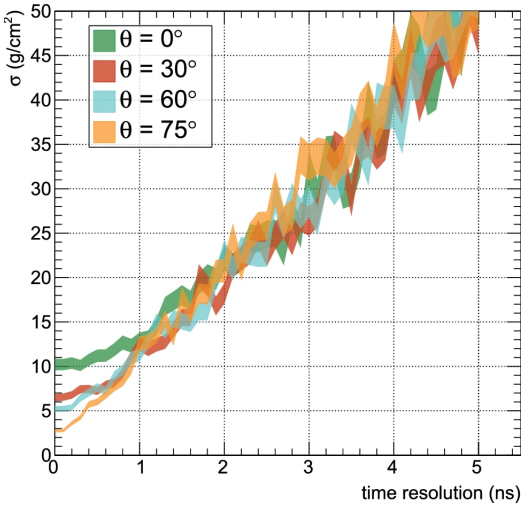

Figure 2.15: The resolution of $X_{\max}$ as a function of the time synchronization between a pair of antennas from simulation [21].

CHAPTER 3

Detection of Cosmic Rays at the Pierre Auger Observatory

As the primary energy of cosmic rays increases, the flux gets suppressed by many orders of magnitude, making it impossible to study the highest energies directly by satellite or balloon experiments, as it is done for energies up to 10^{15} eV. Therefore, ground-based large-scale detector arrays are employed to measure the flux, composition, or anisotropies of cosmic rays by using Earth's atmosphere as a detector volume. The Pierre Auger Observatory is an international facility to study cosmic rays at the highest energies, and it was designed for indirect measurements through the detection of extensive air showers. Secondary particles, produced by interactions of the primary cosmic ray with the nitrogen or oxygen nuclei, can be tracked through the atmosphere due to the emission of fluorescence light and radio waves, or be detected on ground level using dedicated particle detectors. Therefore, Auger employs a variety of different detectors, including water Cherenkov detectors, fluorescence telescopes (FD), scintillation counters, and radio antennas, which play a crucial role in the studies done in this thesis. The radio detector array will be introduced in the following section.

Since the flux drops below $1\,\mathrm{km^{-2}sr^{-1}century^{-1}}$ at energies above 10^{20} eV, detector fields with enormous dimensions are needed to register a sizable amount of events at the highest energies. The observatory covers an area of $3\,000\,\mathrm{km^2}$, which corresponds roughly to the size of Luxembourg, making it the largest detector to study extensive air showers in astroparticle physics. The observatory is located in Argentina, close to the city of Malargüe in the province of Mendoza. It lies on a plateau near the Andes at an altitude of 1 400 m corresponding to a vertical atmospheric depth of $870\,\mathrm{g\,cm^{-2}}$. Figure 3.1 shows a map of Auger, where the location of the experimental site is shown. It includes the positions of the different detector systems operated in the field, the surface detector (SD) and the four FD sites, located at the periphery of the surface array, as well as the Auger Radio Engineering Array (AERA), which lies close to the FD station at Coihueco. Each water Cherenkov detector of the SD is indicated by a black dot. In total, there are 1660 of these SD stations distributed over the $3\,000\,\mathrm{km^2}$ area. The four dark blue dots show the positions of the four sites where fluorescence telescopes are

operated, which together form the FD, located at Coihueco, Los Leones, Los Morados, and Loma Amarillia. There is a Central Campus from which the observatory is maintained. It consists of an assembly building, offices, storage facilities, and the central data acquisition system. The Central Campus lies on a property close to the city of Malargüe [23]. The data taken at Auger is distributed to more than 90 institutions in 18 countries, building a worldwide community. In total, the Auger Collaboration consists of about 400 scientists, engineers, technicians, and students.

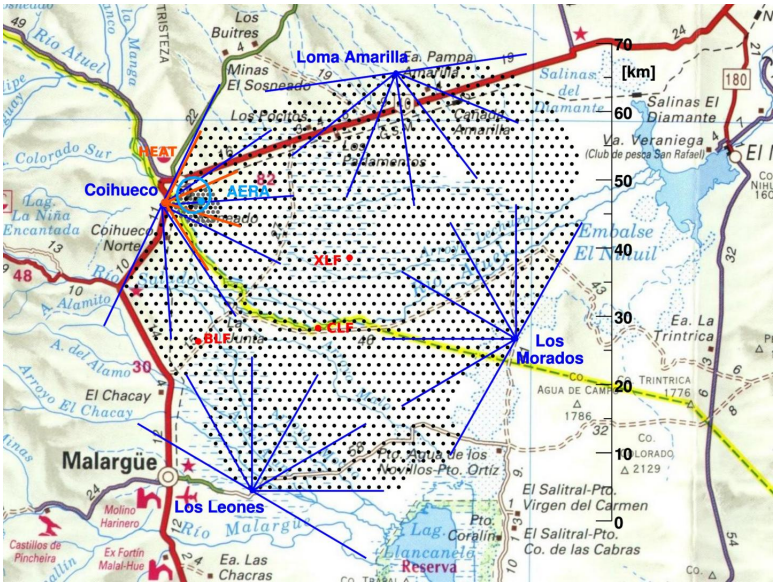

Figure 3.1: A map showing the location of the Pierre Auger Observatory near Malargüe, Argentina, with its expansion of approximately 60 km × 50 km [24]. Each black dot corresponds to a station of the SD, all driven autonomously. Four FD stations are located around the detector array, each of them containing six telescopes with a 30° field of view. The Auger Engineering Radio Array (AERA) is located close to the FD station at Coihueco.

The observatory was conceived in 1991 by physicists Jim Cronin and Alan Watson, to address the nature of cosmic rays at the highest energies. Nine years later, in the year 2000, the construction of the observatory began. Already during the phase of construction, the first physics results were reported, including data from more than 100 surface detector stations, as regular data taking started in January 2004. This was possible due to the modular structure of the detector design, which allows each SD station to operate autonomously. Even though the surface detector was finished in 2008 and is fully operational from that time on, other parts of the observatory are still being upgraded, as is the case with AugerPrime [25, 26]. One of the most significant observations made at Auger is the suppression of the cosmic ray flux above 4×10^{19} eV, which is in accordance with the prediction of the GZK effect, where a steepening of the spectrum was predicted around 5×10^{19} eV [27].

3.1 AERA: Auger Engineering Radio Array

In recent years, as powerful digital signal processing methods became available, the field of radio detection in astroparticle physics has become increasingly popular. The Auger Engineering Radio Array (AERA) is an extension of the detector systems deployed at Auger, specifically designed to investigate radio emission from cosmic ray-induced air showers. It offers information complementary to the well-established methods of particle and fluorescence detection, and provides detailed insights into the electromagnetic component of the air shower, since most of the emission happens here. Similarly to the SD, AERA can operate with a duty cycle approaching 100%. The only limitations of the operating time are weather phenomena where strong electric fields are present in the atmosphere, such as during thunderstorms. However, a technique which is currently under development aims to study lightning using an interferometer made of radio antennas at the site of AERA [28].

AERA is located in the north-west of the observatory, close to the FD site at Coihueco, and covers an area of approximately 17 km^2. In this area, 153 radio antennas have been installed, each of them working autonomously. It was the largest radio detector for cosmic rays before the deployment of the Auger Prime upgrade, which includes a radio antenna at each SD station. The construction of AERA was carried out in three distinct phases. In the first phase, starting in 2010, AERA 1, with 24 antenna stations, was commissioned in a prototype triangular grid with a spacing of 144 m, covering an area of 0.4 km^2. A few years later, in 2013, the array was expanded to a total number of 124 radio stations, distributed over an area of 6 km^2. In this phase, the antenna spacing was increased to a range of 250 m to 375 m, allowing for the detection of cosmic rays with higher energies. The deployment of AERA was completed in 2015, where the last 29 stations were installed at a distance of 750 m [29]. A map of AERA can be found in Figure 3.2. It shows the three phases in which AERA was developed and indicates the position of each antenna within the SD array. On the left, the FD building at Coihueco and the field of view of its telescopes are shown. Coihueco plays an essential role for AERA as the reference beacon is operated from there.

The main component of each AERA station is the radio antenna. Two different types of antennas are installed at AERA, depending on the phase they belong to. While the 24 AERA 1 stations are equipped with Logarithmic Periodic Dipole Antennas (LPDA), all other stations that came later are using butterfly antennas with a span of 2.28 m, mounted on a pole with a length of 1 m. The LPDAs have a span of 4.25 m and a height of 1.8 m. A metal fence surrounds each station to protect the hardware against animals. The signals, registered in the antennas, are, in the first place, amplified by a low-noise amplifier (LNA) which is located directly at the antenna. From the LNA, they are transferred to the readout electronics via a coaxial cable with a length of 2 m. The readout electronics consists of a filter board which applies a 30 MHz to 80 MHz bandpass filter to the incoming signal, and a digitizer unit which creates packages of data that can be transferred to a central AERA-DAQ. As the AERA stations play an important role in the context of the test system developed in this project, they will be described in more detail in the next chapter.

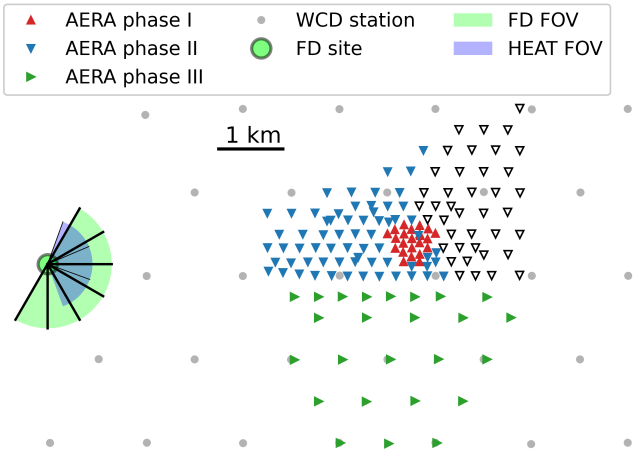

Figure 3.2: A map of AERA from [29]. It is located close to the FD site at Coihueco within the field of the Auger SD and has a size of approximately 17 km^2. Each antenna is marked by a triangle. The array has been deployed in three phases, indicated by the different colors in the map. The water Cherenkov tanks of the SD are marked by grey dots.

The communication with the central DAQ system (CDAQ), where data from the AERA stations is collected, has been realized in two different ways, depending on whether the station belongs to AERA 1 or AERA 2/3. For the prototype phase AERA 1, a network of redundant fiber optic cables buried in the ground has been installed to transfer trigger signals to the antenna as well as data from the antenna to the Central Radio Station (CRS), where all fibers come together. As installing fiber optics over larger distances gets more complicated and especially more expensive, it was decided to switch to wireless transmission of data via a commercial radio communication system with a central base station located at the communication tower at Coihueco. The DAQ can be triggered in two ways. An external trigger can be supplied by the SD, where data is taken in coincidence with the other detector systems at Auger. A second mechanism is provided by a self-triggering algorithm. In essence, this is a simple voltage threshold where signals above a certain threshold are triggered. However, artificially created radio-frequency interference (RFI) can also trigger a station. In order to suppress these RFI, further conditions, primarily related to the isolation of the pulse, must be fulfilled to register a signal as an event. The software at the CDAQ receives the triggers at regular intervals. If coincidences between multiple stations close to each other are detected, the ADC data from all stations are requested and stored at the CDAQ [30].

Recorded radio data is analyzed offline to extract the same quantities as the other detection methods: arrival direction, energy, and mass of the primary particle. The direction of the shower axis is calculated from the arrival times of the signals in the radio antennas. To reach resolutions better than 0.5°, it is necessary to take into account the actual shape of the

shower front, which is hyperbolical. Furthermore, the amplitude of the signal can be used for energy reconstruction as it scales linearly with the energy of the primary particle. To prevent intrinsic fluctuations from reducing the precision of the measurement, AERA employs an approach where the signals are fitted to a model of the radio-emission footprint, provided by simulations. Those footprints are further integrated to get the total energy radiated by the shower. Since the radiated energy scales quadratically with the primary energy, this can be used for energy reconstruction. The most challenging part is the reconstruction of the shower maximum X_{max}. It is usually reconstructed from the lateral distribution of the radio footprint on the ground [19]. However, as mentioned above, interferometric techniques have the potential to improve the reconstruction significantly. An analysis of AERA data using radio interferometry yielded results similar to the reconstruction with classical methods [31].

3.2 The AERA Beacon

As mentioned above, the precise timing of individual detector stations is indispensable to reveal the full potential of reconstruction precision. Unfortunately, timing information based on GPS, like the one used at Auger, only provides accuracy in the range of 5 ns. In experimental data taken at AERA, it has been shown that GPS-based timing can drift even more, leading to relative timing differences of the order of a few tens of nanoseconds [32]. In order to correct for these drifts, a reference beacon has been developed in [33] to provide additional timing information.

The AERA beacon is a transmitter of continuous sine waves, located at the communication tower at the FD site at Coihueco. It is transmitting at four different freuquencies: 58.887 MHz, 61.523 MHz, 68.555 MHz and 71.191 MHz. The frequencies have been chosen, such that they are all within the 30 MHz to 80 MHz range of the bandpass filter which is used in the AERA readout electronics. Four temperature-controlled crystal oscillators with a frequency stability of 10^{-6} per year are combined with adjustable amplitudes before the beacon signal gains a final amplification and is transmitted via a SALLA antenna, which can be seen in Figure 3.3. Each frequency can be individually turned on or off to provide modularity of the beacon signal. The circuitry to control the beacon can be seen in Figure 3.4. The superposition of the four frequencies results in a periodicity of approximately 1.1 µs and any combination of three of them allows for corrections of drifts up to ±80 ns. As the beacon is permanently transmitting, its signal can be seen in the data recoded with AERA antennas. During the analysis of the data, the beacon frequencies are isolated by extracting them from the recorded signal trace via a Fourier transformation. With the information about the phase of the beacon at each station and the knowledge of the exact positions of each antenna, an arbitrary reference station can be picked, and expected time delays to the neighbouring stations are calculated. Furthermore, the predicted time delay is compared to the one measured with the beacon signal. This allows to determine an offset that can be used to correct for GPS drifts. Measurements of the recorded spectrum in the AERA field after the installation of the beacon have shown that the beacon lines are clearly visible in the data. At the frequencies where the beacon is currently operated, the signal is at least 20 dB above the baseline, which is determined by noise and background signals [33].

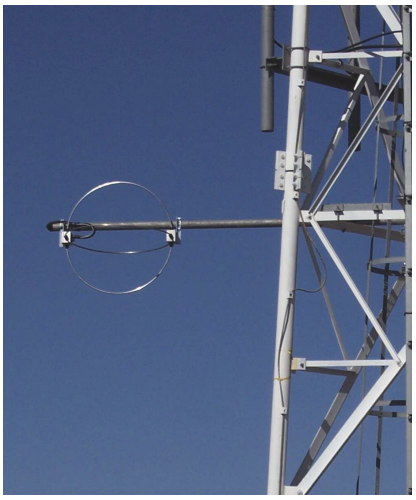

Figure 3.3: The beacon antenna mounted on the communication tower at Coihueco [33]. It is an antenna of type SALLA with a diameter of 75 cm, continuously transmitting sine waves into the field of AERA.

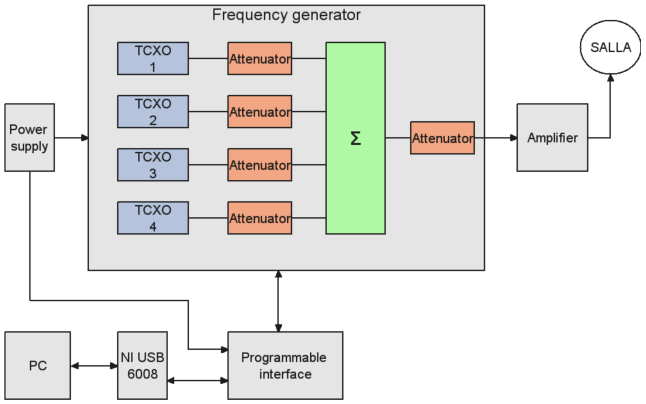

Figure 3.4: Schematics of the beacon system from [33]. Four sine waves are generated by crystal oscillators and further combined and amplified. A computer is used to control the system and to regulate the power at which each frequency is transmitted.

In addition to the beacon-based corrections, an independent cross-check using signals from commercial airplanes has been performed. The airplanes transmit position broadcasts as well as radio pulses, which were detected by the AERA antennas. By comparing the measured arrival times of these pulses to the expected times calculated from the known airplane positions, the timing calibration provided by the beacon is independently verified. These studies confirm that the beacon achieves a synchronization accuracy of about 2 ns or better, demonstrating its suitability for continuous, event-by-event correction of GPS drifts in the recorded data [32].

As the surface detector is currently undergoing the AugerPrime upgrade, each SD station, along with upgrades on the readout electronics, has been equipped with a scintillation detector and a radio antenna on top of the water Cherenkov detector, scaling the radio array from 17 km^2 to a size of 3 000 km^2 [34]. Most recently, in July and August 2025, two new beacons, made of dipole antennas, were temporarily installed at Coihueco and Los Leones [35]. Each of them is transmitting a monofrequent sine wave. The new beacon at Coihueco is running at 50.4 MHz while the one at Los Leones is operating at 50.315 MHz. At least one of them can be seen at every station of the new radio detector RD, which is installed as a part of the AugerPrime upgrade.

CHAPTER 4

The Test System for the AERA/RD Beacon

Even though the beacon at AERA has been deployed over 14 years ago in 2011, it had never been directly tested using a cabled, external timing source. With the upcoming methods like radio interferometry or interferometric lightning detection, sub-ns synchronization between autonomous radio stations is required to reveal their full potential. In addition, with the AugerPrime upgrade and the associated installation of radio antennas on each SD tank, new challenges are coming up concerning synchronization on scales that correspond to the distance between two SD stations, which are 1.5 km apart. The footprint of an air shower initiated by ultra-high-energy cosmic rays reaches a size of up to several 10 km^2 and increases when the shower axis has a large zenith angle. Therefore, several tens of stations can be triggered by such an event. To verify that the beacon synchronization is working and still delivering high-accuracy timing information on that scale, we developed a dedicated test system based on the precise coincident readout of multiple radio antennas using an external timing signal. This allows us to investigate the beacon signal at different positions at the same time and to apply offline signal processing methods to determine the stability of phase differences. The test system has been designed in a way that it is highly flexible regarding the location where it is operated and the number of antennas used in the setup. A minimum of two receivers is needed to perform the analysis on the beacon signal, where one serves as a reference station, and at least one station (more receivers are possible) that is compared to the reference station, to measure phase stability. The test system can be divided into two parts: a transmitting part and a receiving part. The transmitting part consists of a dipole antenna and a signal generator, which provides a sine wave used to drive the beacon. By design, the beacon developed in the context of this project only allows transmitting one frequency at a time. The receiving part, on the other hand, consists of three butterfly radio antennas, dedicated readout electronics, and a laptop for DAQ. The individual components of the system will be described in more detail later in this chapter.

The method applied to assess the beacon stability is based on the assumption that the runtime of the signal from the transmitter to the receiver is constant, as it is expected from the unchanged geometrical distance between both antennas. However, under real conditions the refractive index of air, which is usually given by a mean value for a specific route, is not necessarily uniform on the path between the beacon and the receiving antenna. The test system offers the opportunity of studying these changes in the refractive index by measuring phase differences at fixed positions over a period of time.

Coincident readout of antenna signals is the central aspect for investigating the synchronization between the different antennas. It is essential to mention that the test system is a cabled setup and cannot be operated on stations that are working autonomously. However, the system should not be installed permanently, but serve as a temporary indicator from which conclusions can be drawn on the autonomous stations. During the work of this project, coincident readout has been realized in two ways. In the first stage of the development, a four-channel oscilloscope with a sampling rate of up to 8 GHz has been used to collect signals from up to 3 antennas. Later on, the readout electronics have been switched to discarded AERA digitizers to avoid potential obstacles if the system is transferred to Argentina to be operated in the Auger field. In the course of this change, the White Rabbit network was also implemented in the test system. This has several tasks: it is used for timing the readout at the three digitizers, it provides a synchronized signal for offline corrections, and it enables the data transfer from the digitizers to the laptop, where everything is collected and stored. Therefore, it plays a significant role in the design as it serves as the system's centerpiece.

4.1 The Beacon System

For the design of the beacon antenna, the choice fell on an electric dipole with two arms, which is fed symmetrically at its midpoint. A dipole antenna is a simple and widely used type of radio antenna that is essentially a straight conductor of a length that is in the order of the wavelength to be transmitted. It is one of the most important types of antennas since wireless transmission of electrical signals became common practice. Since the properties of the dipole antenna could be determined early on by analytical calculations, it is used today as a reference antenna to describe the antenna gain of other geometries.

The gain is one of the key parameters used to describe the performance of an antenna, which combines directivity and radiation efficiency. It is a measure of how strongly an antenna radiates in different directions and can be illustrated in a radiation pattern. The gain is calculated from

$$G = \eta \cdot D \tag{4.1}$$

where η is the efficiency and D the directivity of the antenna. It has no units and is usually expressed on a logarithmic scale in decibels (dB). The efficiency is the ratio between the total power radiated by the antenna and the power that is fed to the terminals of the antenna, taking into account the losses that are converted into heat due to the resistance of conductors and absorption in a dielectric medium. However, what is not taken into account here are losses

originating from reflection, which occur if the impedance of the generator does not match the impedance of the antenna. The directivity, on the other hand, is a geometrical property. As for every real antenna, the radiation intensity depends on the direction in space, and there is a main radiation direction where the radiated power is the largest. The ratio of the maximum and the average radiation density is called the directivity.

The antenna used for the beacon is approximately a $\lambda/2$-dipole, where the total length of the antenna arms corresponds to half of the wavelength of the radiated sine wave. Such a dipole, assumed to be lossless, has a gain of 2.15 dB, which means that the power radiated in the main direction is about 64% above the average. As the AERA beacon is operating at multiple frequencies, and hence different frequencies were tested during the development of the test system, the beacon used in the context of this project is not perfectly adjusted to meet the length of $\lambda/2$. However, this does not significantly affect the radiation pattern. In general, a dipole radiates radially around its expansion direction. The radiation is strongest in the plane perpendicular to the dipole axis, and decreases towards the axis. Along the dipole axis, the radiated power reaches its minimum. For an ideal dipole, this would be zero, meaning that no power is radiated along the dipole axis. The radiation pattern is often referred to as a *donut* shape. An example of such a characteristic pattern has been simulated using Numerical Electromagnetic Code (NEC). NEC simulations offer powerful tools for studying the behavior of a wide range of antennas and can be utilized to optimize the geometry for a specific application. An example of such a simulation is shown in Figure 4.1. It shows the horizontal radiation pattern of a dipole antenna oriented along the y-axis with a length of 0.89 m per arm. In total, this corresponds to a $\lambda/2$-dipole, optimized for the transmission of a 80 MHz sine wave. A correction factor of 0.95 has been applied to shrink the length of the antenna to account for the finite thickness of the wires used in its construction. Additionally, a simulation of the antenna gain in the direction of its maximum has been conducted for two different distances from the ground. Here, the frequency at which the antenna is operated has been swept over a range of 30 MHz to 90 MHz. The result shows that the antenna gain is rather constant over a broad range of frequencies, resulting in a plateau with a width of approximately 30 MHz. Furthermore, it can be seen that the position of the plateau changes with the distance of the antenna above the ground. The further up the antenna is installed, the more the plateau shifts towards lower frequencies. This can be seen in Figure 4.2.

In practice, an antenna with a length of 2 m, i.e. 1 m per arm, has been built out of two metal rods, mounted in a plastic housing. The arms of the antenna are made of aluminum and have a diameter of 6 mm. Even though aluminum has a slightly worse conductivity compared to copper, which would have been the alternative material to build the antenna, this difference is barely relevant for the electrical performance of the antenna. The more important aspects are the mechanical properties of aluminum in comparison to copper. Aluminum is lighter (ca. 2.7 $\mathrm{g\,cm^{-3}}$ compared to 8.9 $\mathrm{g\,cm^{-3}}$ for copper) which makes the antenna mechanically more stable and more resistant against wind than an antenna made of copper with the same geometry. Furthermore, instead of corroding over time, like it would happen for copper, aluminum creates an oxide layer that acts as a protective shield. Finally, it has been chosen because it is cheap, easy to procure and process, and there are no disadvantages for the overall performance of the antenna.

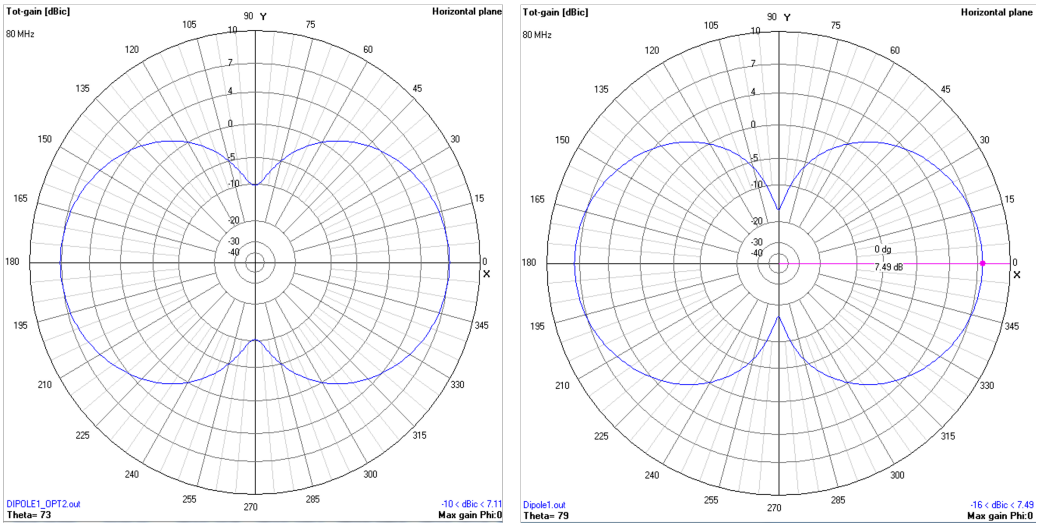

Figure 4.1: The far field pattern of a dipole antenna in the horizontal plane at two different heights, simulated using NEC. The antenna is aligned along the y-axis. In the left panel, the antenna is positioned at a height of 3 m, and in the right panel, it is positioned at 5 m. If the antenna is placed higher above the ground, the radiation along the extension of the dipole becomes suppressed. In contrast, the radiation perpendicular to the dipole gets stronger, which increases the directivity. This is due to the interference of the direct and the ground-reflected wave.

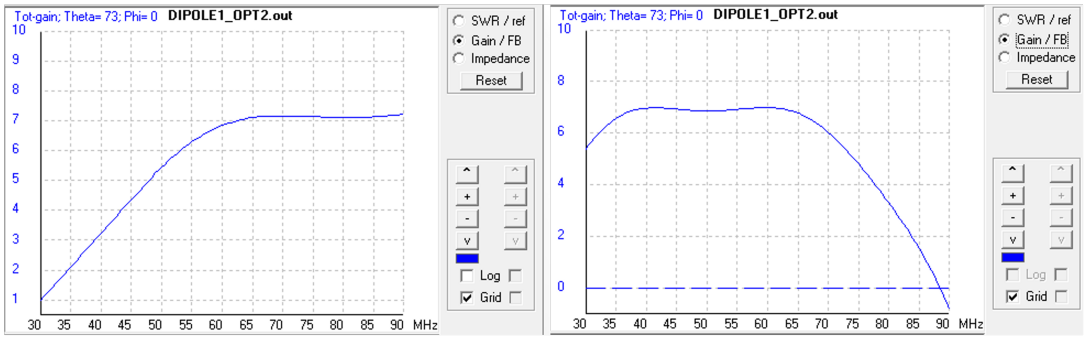

Figure 4.2: The antenna gain of a horizontally aligned dipole in the direction of maximum emission as a function of the frequency. In the left panel, the antenna is placed 3 m above the ground, and in the right panel, it is placed at 5 m. Moving the antenna further above the ground shifts the plateau where the gain is approximately constant to higher frequencies and closer to a value that corresponds to $\lambda/2$. In general, the dipole shows a broadband behavior over a range of 30 MHz.

At one end of each arm, a 2.7 mm hole has been drilled centrally in the rod into which a M3 thread has been cut. These holes were made to connect the transmission line of the signal to the antenna. A cable with a proper connector was fixed at each rod with a screw, allowing for easy assembly and disassembly. Mechanical stability is ensured by a 3D-printed plastic casing made of two parts, a housing and a lid, which also protects the terminals of the antenna against splash water. Four screws, countersunk with nuts, connect the two parts. To provide further mechanical stability, a foam insert has been made, which is placed between the housing and lid, putting pressure on the arms of the antenna and hence restricting the mobility of the parts. There is an insulating gap between both arms of the antenna enclosed by plastic to avoid electrical contact. However, this gap is small compared to the total length and does not change the radiation properties significantly. At the bottom of the housing, there is a hole to feed the signal to the antenna. For this purpose, a female BNC bulkhead connector with a solder cup terminal has been attached and fixed with a flat nut. This connector has two connections that have been soldered to the wires coming from the antenna arms. The 3D-printed casing and the electrical connections inside can be seen in Figures 4.3 and 4.4.

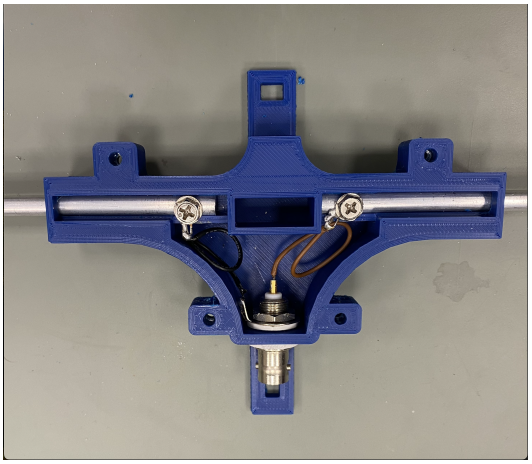

Figure 4.3: Implementation of the beacon antenna. The center-fed dipole is made of two aluminum rods with a length of 1 m each and a diameter of 6 mm. A 3D-printed housing ensures mechanical stability and provides a terminal to connect the signal via a BNC cable.

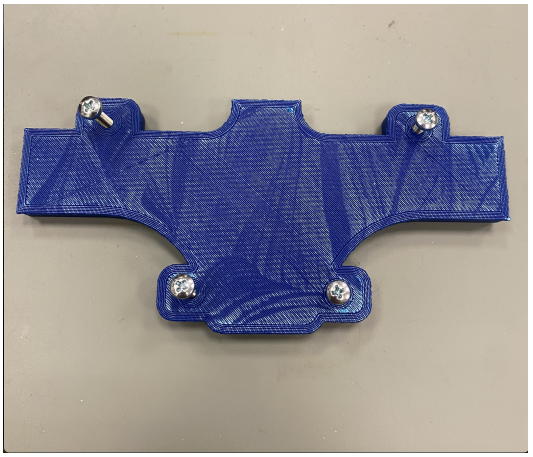

Figure 4.4: Lid of the beacon antenna housing. A 3D-printed cover to protect the electrical connections inside the housing.

The beacon is mounted on a tripod with a telescopic pole, which can be extended up to a height of 2.65 m. This makes the location variable, and the tripod allows for a solid stand even on uneven ground. To provide the beacon signal that should be transmitted, a signal generator of type 33250A from Agilent is connected via a coaxial cable. This device can generate sine waves, squares, and pulses, among other waveforms. The output amplitude, specified for a 50 Ω termination, can be adjusted between 10 mV_{pp} and 10 V_{pp}, with an accuracy of 5% in the operating range used in this experiment. Here, V_{pp} referes to the peak-to-peak voltage of the waveform. The signal generator is connected to the antenna via a 50 Ω coaxial cable, and the amplitude and frequency can be adjusted at the device via a control panel.

4.2 Receiving Butterfly Antennas

To record the beacon signal, a corresponding receiver system is required. In the case of the test system, the signal is picked up by a set of butterfly antennas. Like the beacon antenna, the butterfly antenna is a dipole, with the difference that its arms have the shape of a triangle. The span of such antennas is typically of the order of $\lambda/2$, similar to the beacon antenna. This type of antenna is often used as a broadband receiver. In contrast to the beacon, the receiver is equipped with an active antenna. This means that the antenna signals are not directly fed to the readout electronics, but are first amplified in a low noise amplifier (LNA). The impedance of the antenna is not constant, but changes with the frequency received, which influences the antenna's response to different parts of the spectrum. However, the LNA takes this into account, and, in addition to amplifying the signal, also ensures adaptation to the impedance of the connected cable. The antennas used here were originally used in the CODALEMA experiment [36]. The centerpiece of the LNA is the LONAMOS chip, which was specially designed for this purpose. During the development of the antenna, the gain of the LNA has been determined by connecting a 10 pF capacitor to the differrential input of the LNA [37]. The measurements have shown that the gain of the LNA is at 30 dB with a bandwidth ranging from 80 kHz to 230 MHz.

The housing of the antenna contains an LNA board with two channels. This allows us to measure the two polarization directions, North-South and East-West. However, as only one beacon with a fixed orientation has been used in the studies of the test system, the signal can only be seen in one polarization. Therefore, the antennas have been operated on only one channel. The signals, amplified by the LNA, are fed outside the plastic casing of the antenna, where they can be accessed via an N-type connector. An adapter was mounted on the N-type connector to convert the terminal to a BNC type. From there, the antenna signal is connected to the readout electronics via a 50 Ω coaxial cable. A drawing including dimensions is shown in Figure 4.5.

Since the antenna is active, it must be supplied with a DC voltage of 5 V to power the LNA. This is realized by phantom power via the signal line. Fortunately, since AERA antennas are active too, the digitizers used at AERA provide this phantom power at the input of their filter boards. However, if the antenna is not read out by dedicated electronics like AERA digitizers, but with an oscilloscope, as was done in some of the measurements performed in the context of this project, phantom power must be added to the signal line by an external source. For this purpose, the electronic laboratory of the physics department has developed a circuit board to provide the power needed to drive the LNA. This board is equipped with three BNC connectors: a DC input which can be fed with voltages in a range of up to 12 V, a signal input where the active antenna is connected, and the phantom power is provided, and an output where only the radio frequency part is present. On the board, there is a voltage regulator whose output can be adjusted via a potentiometer. A picture of the board can be found in Figure 4.6. With the help of these boards, it was possible to read out the signals from the butterfly antennas using an oscilloscope. When the readout later changed to AERA digitizers, this board was no longer needed, as the filter board supplies the necessary voltage.

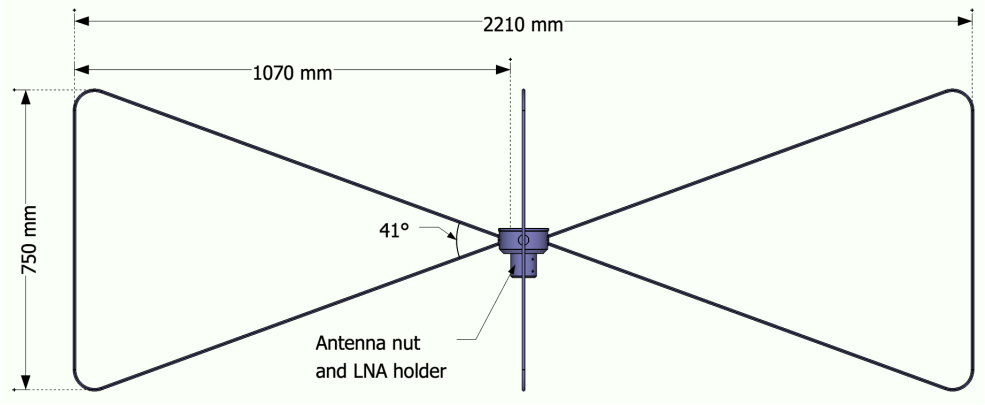

Figure 4.5: A sketch of the butterfly antenna used to receive the beacon signal [38]. The design allows mounting two antennas perpendicular to each other to record two polarizations. Only one was used in the measurements conducted in the context of the test system, as only one beacon was operated. An LNA is mounted inside the plastic holder where the arms of the antenna are attached. Two N-type connectors are available on the bottom of the holder to pick up the signal.

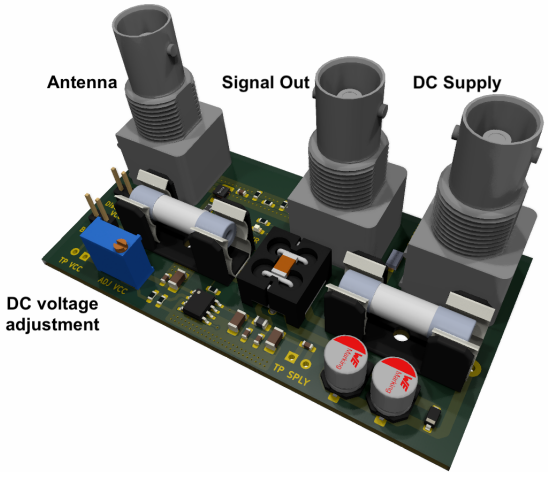

Figure 4.6: The 3D design of the board that is used to supply the LNA of the butterfly antennas with DC power. It has three BNC terminals: One for the DC input, one for the output of the RF signal and one that is connected to the antenna. The board is enclosed in metal boxes with corresponding drillings for the BNC terminals [39].

The mechanical structure of a butterfly antenna is mounted on a metal pole, made of aluminum with a length of 1.25 m. The pole has four holes with threads, which are used to fix the antenna and the housing using screws. Furthermore, there is a larger hole in the pole, which is used to route the signal line from the inside to the outside, where it is connected to the readout electronics. An additional aluminum sleeve was inserted at the lower end of

the pole to reduce its diameter. This allows the antenna to be attached to a tripod, similarly to the beacon antenna. The tripod has a bracket with an adjustable diameter on which the antenna can be mounted and clamped. This ensures mechanical stability and enables flexible positioning of the antenna at different heights. The signal cable must be attached to the BNC adapter before the antenna is mounted to the pole. Otherwise, it is no longer possible to access the connectors. On the top side of the antenna nut and LNA holder, there is a lid that covers the electronics inside. A gasket is placed underneath the lid, which is later fixed with screws to make it weatherproof. In the context of the test system, three butterfly antennas were deployed to pick up the beacon signal at three different positions.

4.3 Oscilloscope-Based Readout

In the first version of the test system, the butterfly antennas were read out by a digital oscilloscope. The device used for this purpose is an HP Infinium oscilloscope of type 54845A. It has a bandwidth of 1.5 GHz and can be used on up to 4 channels at a sampling rate of 4 GSa/s or in a two-channel mode where the sampling rate can be increased to 8 GSa/s. This allows an ultra-fast probing of the signal in the sub-ns range. The 4 inputs are equipped with a BNC terminal, and the input resistance can be switched between 50 Ω and 1 MΩ, which is useful to probe signals without disturbing them. However, the oscilloscope was not only used to read out the butterfly antennas, but also for measurements where the behavior of the LNA or the characteristics of the White Rabbit system were investigated. A dedicated software to read out the oscilloscope with a computer has been provided by the electronics laboratory. The software is running on LabVIEW and provides a graphical user interface (GUI) to select a specific set of channels, set a trigger level, and determine the trigger edge. Besides that, the software has three graphical panels to display the course of the signals and information about the time delay between signals. The time delay is shown in two ways: a histogram of Δt for a given pair of channels, e.g. channel 1 and channel 2, and the time dependence of the same values. Approximately every 2 seconds, a new measurement is taken and displayed. At the same time, time differences are calculated, and the histogram as well as the delay-over-time-plot are updated. This provides the user with fast feedback on how well two or more signals are synchronized. A screenshot of the GUI can be found in Figure 4.7.

If one or several of the save buttons in the LabVIEW application are activated, the corresponding data is stored in external files. In case of the waveforms, which are the most important ones for further offline analysis, the data is saved in so-called *lvm* files, which stand for LabVIEW Measurement File. This is a special text file format, which is created by LabVIEW if measured data is stored externally. It is ASCII-based and hence readable with usual text editors. These files contain a header section, where metadata like date, units, sampling rate, and much more is stored, followed by the measured values. The values are voltages and time stamps, which are saved in tabular form. Although the software allows for changing some settings related to data acquisition, essential parameters such as the number of samples or scaling of the x- and y-axes are not available and must be adjusted directly on the oscilloscope's control panel.

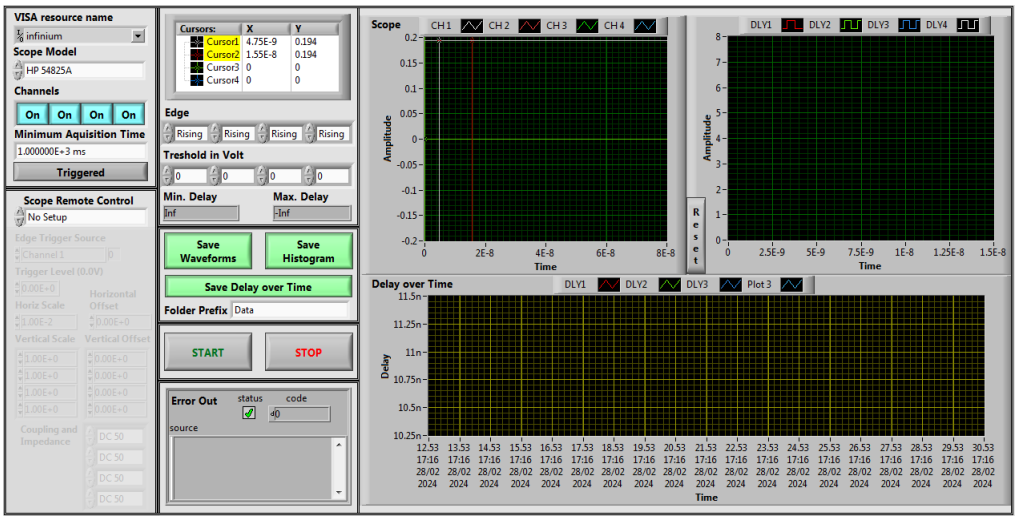

Figure 4.7: A screenshot of the LabVIEW software that is used to read out the oscilloscope. Channel selection and preferences for the data acquisition can be done within the GUI. The software provides almost instantaneous feedback on the signal shape and the timing between different channels of the oscilloscope. Furthermore, data can be stored in external files for offline analysis.

4.4 AERA Digitizers

During the development of the test system, the readout electronics underwent a change. Instead of with an oscilloscope, the antennas were read out by digitizers, which were previously used in AERA and were developed in [40]. These digitizers read out an analog signal from the LNA and convert it into digital data using fast ADCs after it has been passed through a filter board, which also amplifies the analog signal. The filterboard was developed at KIT and is designed for a bandwidth of 30 MHz to 80 MHz, which is the frequency band that AERA uses. Besides the analog processing of the antenna signals, it also provides the supply voltage for the LNA. This is done via a bias tee, which is a three-port network that adds a DC bias voltage to a radio frequency signal without disturbing other signals in the circuit. The bias tee allows powering the LNA on the same line where the signal is propagated. At the circuit board of the LNA, both signals have to be split again.

Each filterboard has four outputs, two for the signal in the East-West channel and two for the North-South channel. This is because the filterboard applies two different gains to the signal. One is referred to as the low-gain channel, and the other is the high-gain channel. Between low-gain and high-gain, there is a difference of 10 dB in the amplification. Since the filterboard is a separate PCB and not integrated on the main PCB of the digitizer, it is connected via a set of pin headers. Furthermore, four spacers that can be screwed to the bottom side of the filterboard are used to ensure mechanical stability. The actual circuit of the filterboard is enclosed in a metal housing to protect it against RFI. There are two versions of the filterboard available, which have both been used in the context of this project.

The older version has two physical inputs, which are separated into high-gain and low-gain on the board. This enables the simultaneous reading of the low-gain and high-gain values of one channel. However, the newer version of the filterboard does not allow for this anymore. Here, low-gain and high-gain are already separate inputs, where either one must be chosen. The connectors at the input are of type SMA and are fed through the back panel of the digitizer casing. Pictures of both versions of the filterboard can be found in Figures 4.8 and 4.9.

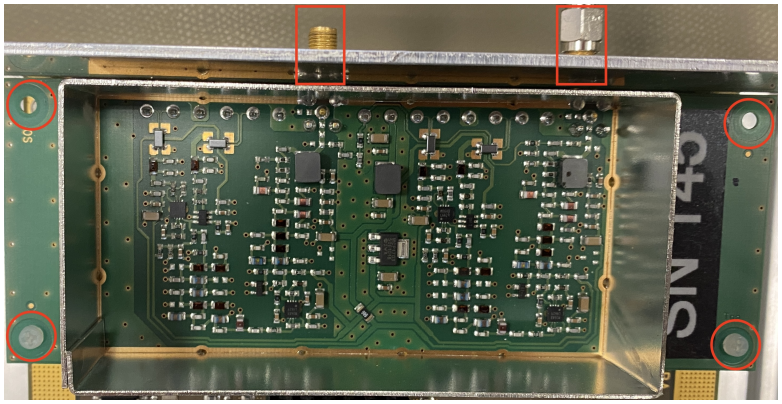

Figure 4.8: Filterboard for AERA Version 2 digitizers. It features two SMA inputs, marked with red boxes, and four holes where spacers can be inserted for mechanical support (red circles).

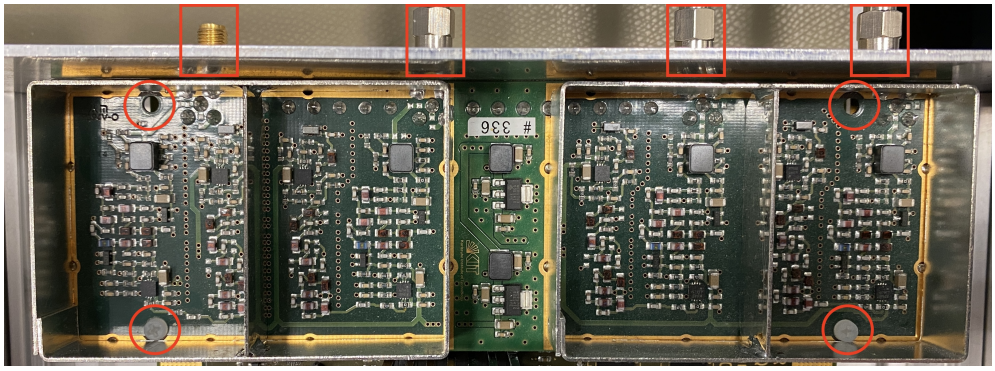

Figure 4.9: Filterboard for AERA Version 3 digitizers. These boards have four SMA inputs, indicated by the red boxes, and also four holes for mechanical support (red circles).

Coming still as analog voltages from the filterboards, the signals are then digitized by four ADCs of the type AD9629. These ADCs have a sampling rate of 180 MHz and a 12-bit resolution, which results in output values between -2048 and +2047, carried out at a time interval of 5.555 ns. The ADCs are supplied with an external clock that provides the 180 MHz, and the data is continuously streamed into an FPGA from the Cyclone III series from Altera. This FPGA is used for triggering and applies algorithms for the processing of the

ADC data with low power consumption. Online Fourier transformations and digital filters can be applied in real time. To temporarily store the ADC data on the digitizer, a 4 GB SDRAM module (SODIMM) is mounted on the digitizer board. This allows a buffer of about 7.4 s of data if two channels are read out simultaneously. For the permanent storage of data used by the FPGA, a 4 GB iNAND memory chip is soldered on the digitizer. On the bottom side of the digitizer board, a GPS module is installed. The GPS module is a separate PCB and, like the filterboard, it is connected to the main board via a pinheader and four plastic screws for mechanical support. The module receives data from GPS satellites and internally generates a PPS signal. This clock, along with additional information about the status of the GPS signal, is forwarded to the FPGA and marks the intersecond boundary. Furthermore, the additional information delivered by the GPS module allows the DAQ to correct for offsets in the starting point of the PPS signal. A GPS antenna can be connected to the front panel of the digitizer's casing. The PPS coming from the GPS board plays a key role in the whole DAQ system, as it serves as the reference timing signal. However, to get even better timing than what can be achieved by GPS, in the development of the test system, the PPS has been replaced by an external source, which will be described later in this thesis. All the different subsystems on the digitizer must be supplied with different voltages. The main voltage supply is provided through a terminal on the front panel of the digitizer to which 12 V must be applied. This voltage is converted in two steps, using a set of DC-DC converters. In a first stage, a voltage of 3.3 V is generated, which is used to supply digital components like drivers or the GPS module. Furthermore, this voltage is converted to even smaller values between 2.5 V and 1.8 V, which are used to power different parts of the FPGA. The analog parts are supplied by a separate voltage branch. Here, 6 V are generated to drive the filterboard, which is then reduced to 1.8 V to power the ADC inputs. The electronics of the digitizer are enclosed in an aluminum housing that can be disassembled into six separate parts. The main PCB is mounted on the baseplate of the housing, spaced by two aluminum bars. These bars have a width of about 1 cm to increase the contact area with the PCB and are used to dissipate heat. On the back panel, there are holes to feed the SMA connectors from the filterboard, where an antenna or another signal source can be applied through the housing, which are tightened with washers and nuts. All the other connectors, like the power supply, Ethernet that is used for the streaming of data and the communication with the digitizer, the GPS antenna, and programming interfaces, are located on the front panel, where the corresponding cutouts were made. A picture of the inside of the digitizer can be found in Figure 4.10.

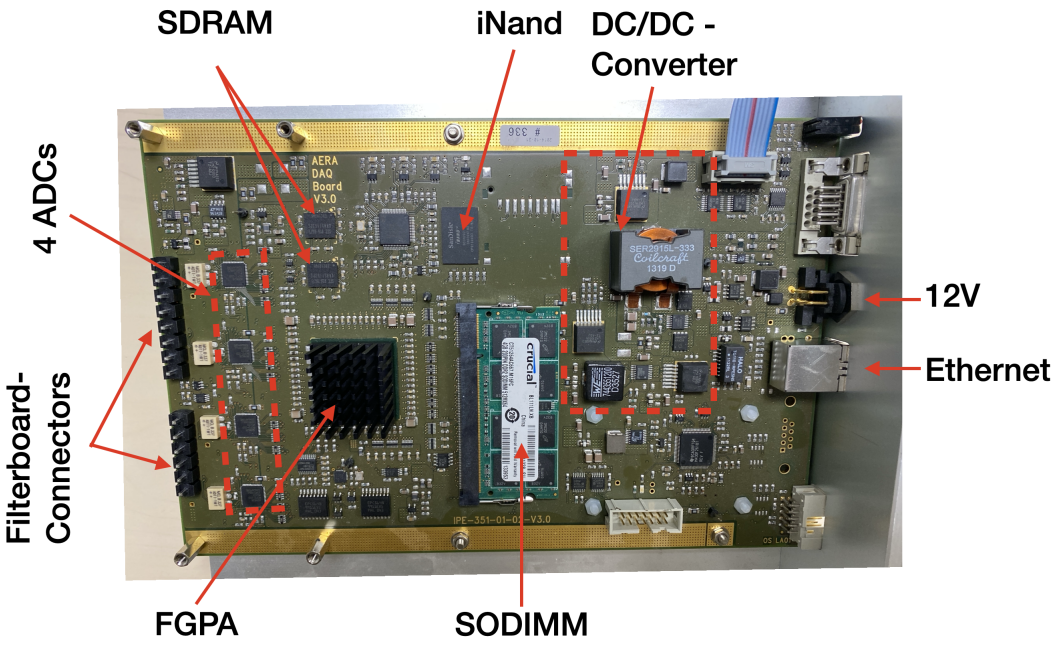

Figure 4.10: The electronics of the AERA digitizer without a filterboard being connected. Mainly responsible for data processing are the four ADCs and the FPGA. The GPS module is not visible as it is located on the bottom side.

4.5 White Rabbit

White Rabbit (WR) plays a key role in the concept of the test system, as it serves as a timing reference for the coincident readout of multiple antenna stations. The technology is an extension of a standard Ethernet network and the IEEE Precision Time Protocol (PTP) to provide time-stamped messages between several nodes of a network and has the capability of gigabit data transfer. It has been developed in a multilaboratory project initiated at CERN to provide a solution for the control and DAQ system. Its firmware and hardware designs are open-sourced and hence freely available, which makes many commercial implementations available. The main features are the precise timing, which allows for sub-ns synchronization, the large scalability with up to thousands of nodes in a network, and the large distance between individual stations, which can range up to several tens of kilometers between nodes using optical fiber cables. This makes it attractive for a variety of applications, including industry, telecommunications, or in specific for the test system developed for the AERA/RD beacon. The system works in a master-slave mode, whose clock frequencies are synchronized using Synchronous Ethernet, which reduces the problem of determining latencies in the synchronization process to the detection of phase shifts, enabling accuracy in the sub-ns range. The Synchronous Ethernet provides a common clock that is shared among all nodes and distributed over the Ethernet physical layer. This ensures that all nodes in the network are operating at the same frequency, which helps to reduce jitter.

The other technology on which synchronization is primarily based is the PTP. However, the standard PTP has its weaknesses due to inaccuracies in time-stamping and delay measurements. Therefore, the PTP has been extended by Synchronous Ethernet for frequency locking mentioned above, an accurate one-way delay modeling, and a WR-specific link setup procedure. Usually, PTP measures the round-trip delay (from the master to the slave and back to the master) and divides it by two to derive the one-way delay. The improved delay model takes into account link asymmetries in fiber optics, which occur when two devices are communicating over a single fiber using different wavelengths for transmitting and receiving. Since the refractive index of the fiber changes with the frequency of the transmitted wavelength, the propagation delay is not identical in both directions. Furthermore, there are fixed delays between the master and a slave, introduced by the transmission and reception delay in the circuitry on both sides of the connection. With the knowledge of the fixed delay and the difference in the refractive index for forward and backward propagation of the signal, the one-way master slave delay can be calculated and fed into the adjustment algorithm of the salve clock. Before timing corrections can be exchanged, the communication and hierarchy in the network must be established. This process is called WR link setup. In this process, it is defined which side is the master and which side is the slave. This step involves an announcement from the master, followed by an answer from the slave that it is present. When the master received the answer, it tells the slave to lock its clock to the one from the master, which the slave also confirms. Now, the master and subsequently the slave calibrate their fixed delays. Finally, the master sends a message to the slave to announce that the link has been successfully established.

Once this is done, the standard PTP messages are exchanged between the master and the slave. This process happens in four steps, where timestamps are exchanged between the master and the slave, which is called a delay request–response mechanism with a two-step clock. At the start of the protocol, the master sends a sync message, and then a follow-up, which contains the time t_1. This message is received by the slave at its local time t_2 and followed by a delay request from the slave. It is sent at the time t_3 and received by the master at the time t_4 in the master's clock system. Finally, the master replies with a delay response message carrying t_4 to the slave. Now, the slave has four timestamps: the master's send time (t_1), the slave receive time (t_2), the slave's send time (t_3), and the master's receive time (t_4). From these four timestamps and the knowledge about one-way delays due to link asymmetries, the slave calculates the master-to-slave delay and corrects itself for the clock offset. The process of applying the PTP is repeated periodically to keep the synchronization [41].

Both, the WR software and the hardware are open-source projects and hence a widely available, customizable, and trusted technology. Ready-made kits for setting up WR networks are available from various providers. In the context of the beacon test system, a White Rabbit Lite Embedded Node (WR-LEN) from the company Seven Solutions is used [42]. The hardware of WR-LEN is based on an Artix-7 FPGA chip to create a compact and entry-level WR system, which was designed to be cost-effective and flexible. It features a dual-port architecture, making it suitable for daisy-chain setups with up to 20 devices. The kit used for the test system consists of three such WR-LEN devices.

On the front side of a WR-LEN, which can be seen in Figure 4.11, there are several connectors and interfaces for communication and clock signals available. There are three SMA connectors, two ports for Small Form-factor Pluggable (SFP) modules, and a Mini-USB connector. The first SMA connector (1) is a clock input, where the WR-LEN can be supplied with an external 10 MHz square wave signal, which then serves as a reference for the internal clock. The second SMA connector (2) is a clock output. A 10 MHz square wave signal can be accessed here, which is synchronized with all other WR-LEN devices via the WR and PTP synchronization. The third SMA connector (3) has two different functions, depending on the configuration in which the WR-LEN is operated. In case it is configured as a grand master, the port serves as an input for an external PPS signal, coming from a GPS receiver, an atomic clock, or something else that provides this type of signal with high precision. Furthermore, in this configuration, a 10 MHz clock must also be provided at the clock input. Both signals must meet the following requirements to be compatible with common logic levels:

- PPS input: 50 Ω, LVTTL (3.3 V logic) or TTL (5 V logic),
- 10 MHz input: 50 Ω, LVTTL, TTL or sine with $[1 - 5]$ V RMS amplitude.

On the other hand, if the station is configured as a usual master, there is a PPS output at this connector. This output is particularly useful for the implementation of WR to the test system as the PPS signal is used to synchronize digitizers.

For the connection of the fiber, there are two ports for SFPs (4) and (5), which serve as both, the transmitter and receiver of optical signals simultaneously. By default, the WR-LEN is configured such that the SFP at the master has to be inserted in slot 2, and for the device to act as a slave, it has to be inserted in slot 1. However, it is also possible to change the assignment of the ports via a command-line interface. Because the communication proceeds via a single fiber, and hence it must be bidirectional, the master and slave must be equipped with different SFPs that are transmitting light at different frequencies. To make the SFPs distinguishable, they are marked with different colors. The purple one, which indicates that the port is configured to be a master, is transmitting at a wavelength of 1 490 nm while the blue one, which must be inserted into the slave port, is transmitting at 1 310 nm. To ensure that communication between the stations can be established, these connections must not be interchanged. A PIN diode, which is sensitive to the corresponding other frequency, is used to receive the light signals on the other side. Like it is the case for most commonly used SFPs, the fiber has to be connected via an LC connector, which has a ferrule diameter of 1.25 mm. Those are highly sensitive and must be handled with care to avoid scratching the surface of the fiber, as this would lead to losses in the data transfer. Above each SFP port, two LEDs indicate the status of the WR-LEN. Once the connection is established, a green LED is permanently on, while the adjacent one blinks with an orange color as soon as there is activity between the stations.

In the bottom right corner of the front panel, a mini-USB connector (6) is located. This can be used to connect a WR-LEN to a PC and communicate with the system via a UART interface to configure the ports for the SFPs to be a master or a salve, or to set the mode of

one station as grand master, where the station is clocked by an external source. However, in the use case of the test system, WR has been used in the standard configuration where the three stations were connected in a daisy chain. Furthermore, the UART interface also allows monitoring the functionality of the network or inspecting log messages, which are generated every second.

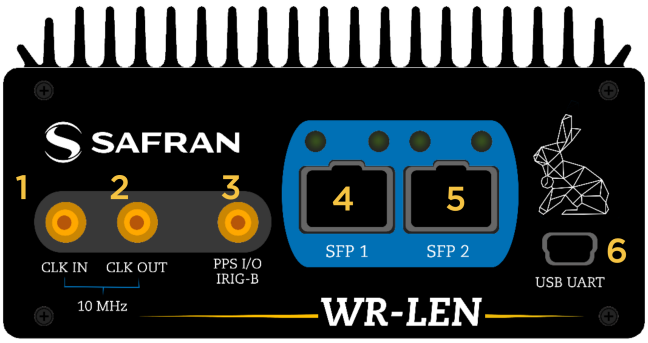

Figure 4.11: Front view of a WR-LEN, like it is used in the test system [42]. Clock inputs and outputs are available, along with two SFPs for the connection to the optical fiber.

On the backside of the WR-LEN, which is shown in Figure 4.12, there are two further inputs, one for the power supply (7) and another one to establish an Ethernet connection (8). The WR-LEN must be supplied with a 5 V DC voltage via a DC barrel jack connector and consumes 7.5 W at most. The Ethernet port can be used to transfer data via the optical fiber in addition to the WR protocol. This functionality has been used to read out the AERA digitizers. A WR signal cannot be accessed via this port.

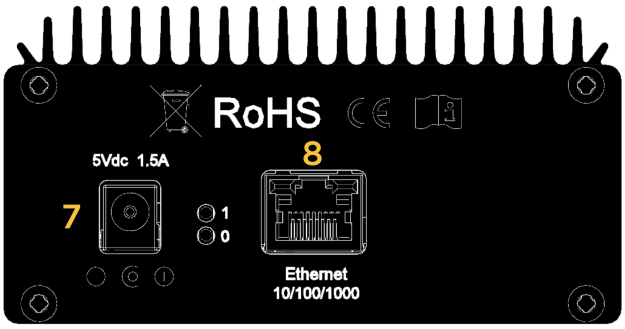

Figure 4.12: Back view of a WR-LEN, like it is used in the test system [42]. The power supply and an Ethernet connection for data transfer via the optical fiber are located here.

4.6 Hardware Modifications to AERA Digitizers

As mentioned above, AERA digitizers are supplied with a PPS signal, which comes from the GPS module mounted on the bottom side of the digitizer. This PPS signal is important for the readout, as it is recorded by the FPGA to mark the start of a new second. But, it is also known that the GPS PPS is not very precise and can drift by several nanoseconds. This, however, is not sufficient for the application of the test system. Therefore, to improve the timing of the PPS, we developed a way to change the source for the PPS signal to an external one, which could, for instance, be connected to a WR-LEN. The GPS PPS and the WR PPS both follow standard logic values, which makes it possible to exchange the input without the need to adapt the signal amplitude. The digitizer, therefore, does not notice from which source it is supplied with the PPS signal.

To realize this external PPS input, the housings of three digitizers were modified, and an additional PCB was inserted between the GPS board and the main PCB of the digitizer. The PCB allows for choosing whether the PPS should come from the GPS board or from an external source by placing a jumper, which can be set in two positions. On the top side of the PCB, which is shown in Figure 4.13, there is a pinheader with 10 pins, matching the size and pitch of the connector GPS PCB to fit on the main board of the digitizer. On the bottom side, which can be seen in Figure 4.14, there are three connectors mounted. A female connector to connect the PPS injector with the GPS board is situated underneath the pin header from the top side. The connector has 10 contacts, 9 of which are simply plated through as they are not needed for the PPS signal. The PPS pin, however, is connected to another pin header with three contacts, which is located on the opposite edge of the board. The middle pin is the common connection, and it routes the PPS to the pin of the connector on the top side, which forwards the PPS to the main board. The other two pins are used to connect either of the PPS sources. One of them is connected to the GPS PPS, while the other one routes the connection to an external input, where a female SMA jack is installed. Just like the GPS board, the PPS injector also has four holes in the corners, which must precisely meet the dimensions of the GPS board. A plastic spacer with a height that corresponds to the distance between the two PCBs, which has been measured to be 9 mm, has been placed in each corner to increase the mechanical stability. Similarly to that, another set of spacers has been inserted between the PPS injector and the main board. The additional PPS injector board led to the PCB sticking out further, which meant that the electronics did not fit into the metal casing anymore. Therefore, the front panel and the back panel of the digitizer were extended by two additional metal plates. Usually, the main PCB is connected to the casing via two aluminum bars with a height of 10 mm, which are also used for cooling. In the adapted design, those bars were not screwed directly to the bottom plate of the casing, but additional spacers of 12 mm were places inbetween. This increased the total height by the same amount. The extensional metal plates were made of aluminum with a thickness of 2.5 mm, similarly to the other plates that enclose the digitizer, and have four holes with a diameter of 4 mm in the corners. The vertical distance between the holes matches exactly the additional 12 mm coming from the spacers, while the horizontal distance corresponds to the distance of the

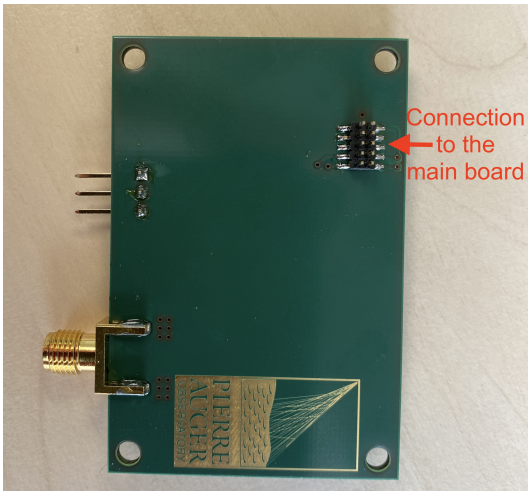

Figure 4.13: The top side of the PPS injector board. This side is connected to the main board.

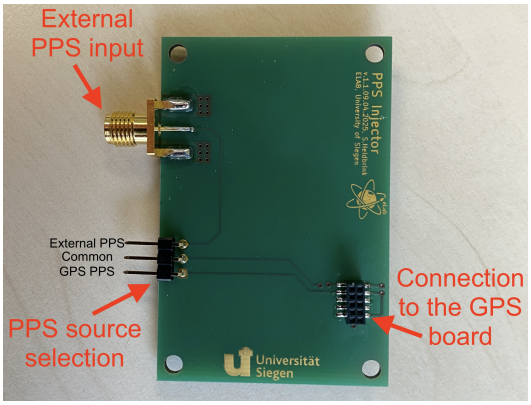

Figure 4.14: The bottom side of the PPS injector board. On this side, there is the jumper for the selection of the PPS source, the SMA connector for the external PPS, and the connector to which the GPS board is connected.

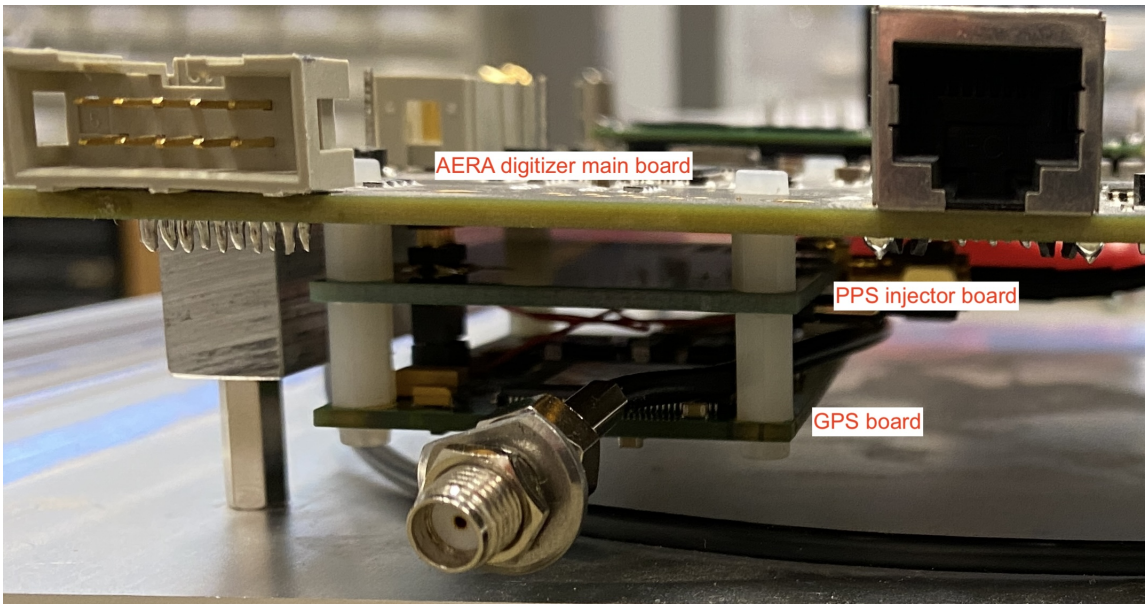

Figure 4.15: PPS injector board installed in a digitizer. The PCB is mounted between the main board of the digizizer and the GPS board. A total of 8 plastic spacers ensure the correct distances between the PCBs.

holes in the original front panel. Furthermore, the side panels also had to be adjusted. A set of two new ones has been produced for each of the casings where the height has been increased. The side panels are not mounted with screws, but are only inserted into rails that are on the edges of the top and bottom plates of the digitizer. To fit into those rails, the side panels have been made of stainless steel with a thickness of 1 mm, which offers a better RFI protection than an aluminum plate with the same thickness.

To access the external PPS injector from the outside of the casing, and because the extensional metal plate on the front panel partially covers the hole where the GPS antenna previously was connected, two new holes were drilled into the front panel. This allows for feeding both SMA connectors to the outside and connecting a GPS antenna and an external PPS source in parallel. Inside the casing, a coaxial cable is connected to the PPS injector. The adapted casing with the new connector on the front panel can be seen in Figure 4.16. In total, three digitizers were extended with the PPS injector board and the additional metal plate at the front and back panels.

Figure 4.16: The front panel of an AERA digitizer that has been modified. A SMA connector for the external PPS input has been added to connect a WR to the digitizer and the position of the SMA input for the GPS antenna has been moved because the extension of the front panel covers a part of the previous hole for the GPS.

4.7 Readout of AERA Digitizers

The signals, which are recorded by the antennas and buffered in the digitizer, are read out via a DAQ software tool, which communicates via a Linux driver with the FPGA and requests the ADC raw data. This data can either be stored in a binary format or, alternatively, in ASCII format and must be decoded by a dedicated program to be usable for data analysis. A single readout is referred to as an event and contains a certain number of samples, arranged in blocks of data, that can be adjusted via a parameter in the readout program. This value can be entered in the command line during execution [43]. In each readout, multiple blocks of data can be acquired, which are either written individually to a file or collected and output as one large file. This is particularly important if the total number of samples becomes large,

which is not the case for the readout performed in the beacon studies. Each block of data contains a specific number of samples, which can be set via an additional parameter. A typical trace that is read out at AERA contains 2048 samples. This corresponds to a trace length of approximately 11.4 µs. The modified software, however, allows for an almost arbitrary length of ADC traces. Further arguments can be entered via the command line, which are listed below:

- dumpMode,
- swChannels,
- daqFillTime,
- requestSecAgo,
- daqBetweenTime.

The dumpMode determines whether the data is stored in ASCII or binary format and defines the structure of the file, i.e. if an event is stored in a single file or in one file per block. Every digitizer has four channels, two low-gain and two high-gain channels. The swChannels parameter selects which of them are read out. All combinations of high- and low-gain are possible in this context. Before data can be read out, the buffer on the digitizer must be filled. Therefore, there is a parameter daqFillTime that defines a time (typically 10 seconds) to wait until the readout starts, to avoid the collection of data from times when the state of the FPGA and buffer was unknown. The requestSecAgo parameter defines the time in the past at which the data is taken. This parameter must stay below a specific value not to exceed the memory limit of the digitizer, and hence, only request data that is still in the buffer. The last parameter is the daqBetweenTime, and it determines the waiting time between two events. This value must be large enough to ensure that the readout of the previous event is completed before the next one starts.

The readout software must be executed on the digitizer itself. Therefore, to perform readouts and to store the data externally, the digitizers are connected to a laptop, which is used to control the system. The communication with the digitizers is established via a telnet session, and for an easy transfer of the data within the test system's network, an NFS share is used. In cases where multiple digitizers are read out simultaneously, communication with the different hosts must be established. This is done in a parallel telnet session, where each host (or digitizer) talks to the laptop from where the readout is coordinated in a separate subshell process. The parallel telnet sessions allow running the readout software on all digitizers at the same time. As already mentioned above, the readout is timed by a PPS signal, which usually comes from the GPS board, but has been replaced by the external source in the development of the test system. To avoid different stations starting the readout at different times, the readout software waits for a common timestamp to be received by the station. A script is used to transmit this timestamp in the User Datagram Protocol (UDP) [44] via netcat to a set of hosts, all of which are addressed in parallel. To avoid that different stations read data from

different seconds, a timeout, which makes sure that the transmission of the timestamp does not take longer than one second, is implemented in the script that sends the UDP packages.

Logging messages in the console are marked with the hostname and the time at the host to check whether all stations were reached and communication could be established. Furthermore, the event number of the current readout is printed together with information about the parameters given to the readout program. This helps the user to monitor the DAQ.

4.8 Final Network of the Test System

The beacon test system has been developed in several stages. For the initial measurements, the readout was done using a single oscilloscope with a large sampling rate, where all receiving antennas were connected. This setup has a limited range, as only BNC cables with a length of 30 m were available for the installation. The switch to AERA digitizers allowed to expand the distance between the stations to an order of magnitude of up to 100 m. At each station, there is a butterfly antenna connected to the LNA, whose signal is fed to one of the analog inputs of the digitizer. To collect the data with the largest possible amplitude, the antenna has been connected to one of the high-gain channels. For one of the digitizers used in the setup, however, this choice became superfluous because it is equipped with a newer version of the filterboard, where low- and high-gain are separated within the filterboard and not directly at the input. In this case, the antenna signal has been recorded in both channels, which does not influence the performance or usability of the test system. Furthermore, a WR-LEN station is placed next to each of the digitizers. The PPS output from the front panel of the WR-LEN is connected to the external PPS input at the digitizer, which has been implemented with modifications of the hardware. This is the key ingredient for the synchronous readout. The antenna and PPS part of the network are the same for all three stations. For the description of further connections in the network, the stations can be classified into one local and two remote stations.

The remote stations have an Ethernet connection going from the digitizer to the backside of the WR-LEN. The ADC data from these stations is transferred to the WR-LEN of the local station via an optical fiber. The fiber also links the three nodes of the WR network. From the local station, one fiber is going to each of the remote stations. At the local station, data is collected by a laptop, which is also used to control the test system. Since every WR-LEN only provides one Ethernet port, a network switch is inserted to which the digitizer and the WR-LEN of the local station, as well as the laptop for the DAQ, are connected. Each digitizer has a fixed IP address, such that they can be addressed individually from the laptop. Concerning the transfer of ADC data, the WR stations serve as converters that convert the data into optical signals and vice versa. The optical link between the stations is established using a single-mode, military-grade fiber cable with LC connectors at both ends. It has a diameter of 4 mm and a length of 250 m. Even though only one fiber is needed per connection in the test system, the cable provides two so that one can serve as redundancy in case the other one breaks. The network is depicted in Figure 4.17.

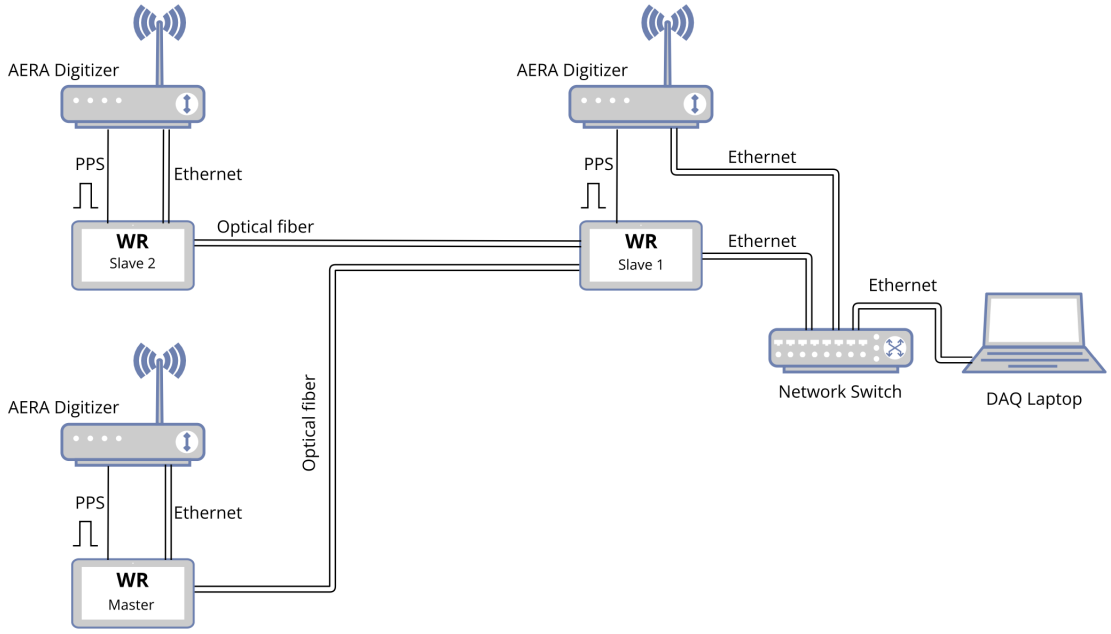

Figure 4.17: A sketch of the network of the test system. It consists of three digitizers, three WR-LEN stations, a network switch, and a laptop. The WR stations are connected via optical fiber, which is also used to transfer the ADC data to the DAQ laptop. The network is expandable by daisy-chaining further WR-LENs and digitizers.

CHAPTER 5

Signal Processing Techniques for Timing Analysis

In the measurements performed with the test system, regardless of the readout method, time series of antenna signals were recorded. In the case of an oscilloscope-based readout, those signals were not further processed before being recorded into a file. On the other hand, when the readout was done using AERA digitizers, the data went through a 30 MHz to 80 MHz band-pass filter. In either case, the beacon signal, which is a monofrequent sine wave, is always contaminated with background signals coming from nearby radio transmitters and noise from different sources. The main idea of the signal analysis is to isolate the beacon signal from all the background and measure the phase difference or time difference between different antennas, located a certain distance apart from each other. This difference should, in principle, stay stable as it mainly depends on the geometrical distance between transmitter and receiver or the distance between the receivers themselves. With the help of the test system, we will determine whether this stability is in the sub-ns range, as needed for interferometric analysis techniques. To extract the stability of the beacon signal from the traces recorded by the antennas, two main signal processing techniques were applied. On the one hand, cross-correlation has been used to directly extract the delay between the signals. On the other hand, the Fourier transformation has been used to obtain the same information from the frequency spectrum of the recorded signal. Both methods measure the same value and hence can be used for cross-checking results. The cross-correlation and the Fourier transformation method are introduced in the following sections.

5.1 Cross-Correlation Analysis

Cross-correlation is a measure of the similarity of two signals, usually time series. It shows how closely their features are related to each other as a function of the displacement of one signal relative to the other. If two signals are identical with no offset, the cross-correlation

function has a global maximum where the displacement between the two curves is zero. On the other hand, if there is a time delay Δt, which is not equal to zero, the peak will be shifted to that delay. For two continuous signals, $x(t)$ and $y(t)$, the cross-correlation is defined as follows:

$$CC_{x,y}(\tau) = \int_{-\infty}^{+\infty} x^*(t) \cdot y(t+\tau)\,\mathrm{d}t. \tag{5.1}$$

In this equation, $x^*(t)$ is the complex conjugate of the signal $x(t)$ and τ is the displacement between the two signals, which can be a continuous value if the signals themselves are continuous. If the signal is discretized, as is the case for all digitized measurements, typically appearing as arrays of a finite size, the integral becomes a finite sum, and the cross-correlation is calculated via

$$CC_{x,y}[k] = \sum_{i=0}^{N-1} x_i^* \cdot y_{i-k}. \tag{5.2}$$

The amount of samples by which the one curve is shifted against the other, k, is often referred to as lag and can take values in the range $[-(N-1), (N-1)]$, where N is the number of samples in the trace. The fact that the maximum of the cross-correlation defines the point of maximum similarity still holds, but there is now a finite resolution, given by the distance between two samples, which is determined by the sampling rate of the recording hardware. In the context of the test system, this technique has been employed to measure the time delay between two signals originating from antennas at different stations. To find their delay, the maximum of the cross-correlation has been determined, and its position k_{max} has been converted to a time offset by multiplying it by the inverse of the sampling rate or the time difference between two samples. The delay Δt is given by

$$\Delta t = k_{\mathrm{max}} \cdot t_{\mathrm{sampling}}. \tag{5.3}$$

This gives access to the time difference of the beacon signal between a pair of antennas, and applying this technique to multiple events provides insights into the distribution of the time delay, which is directly related to the stability of the beacon signal and its accuracy. Figure 5.1 shows the basic principle of this method. In the left panel, the original signals are shown, with a visible time difference. The central panel shows a section of the cross-correlation as a function of the delay, or time lag, and a vertical red line marks the position where the correlation reaches its maximum. In the right panel, the same two signals as before are shown, but in contrast to the first panel, the second signal is shifted by the delay extracted from the maximum correlation. One can see that both signals are now overlapping.

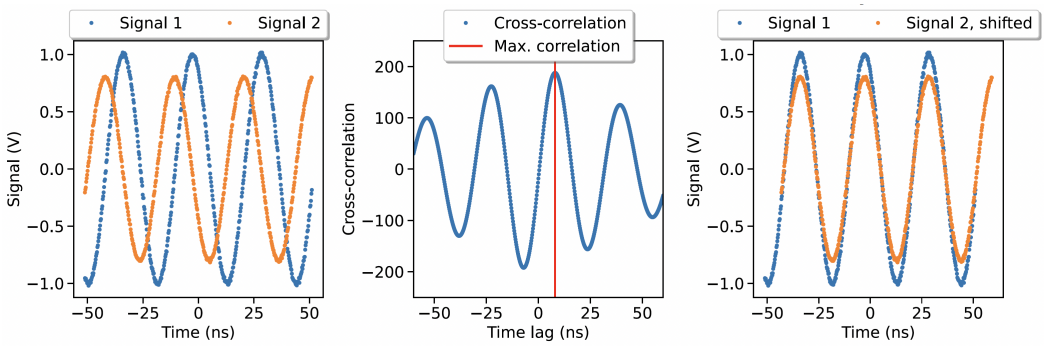

Figure 5.1: A graphical illustration of the cross-correlation technique. The cross-correlation of two signals, which are not in phase, is shown in the central panel. From the maximum of this curve, the time delay is extracted. The right panel shows the same signals, but signal 2 is shifted by the delay determined from the cross-correlation. As a result, both signals are perfectly aligned.

5.2 Fourier Transformation

Another approach to measure the time delay between two signals can be done via the frequency domain. It can be proven that every periodic signal can be decomposed into an infinite series of sine and cosine functions, which is called the Fourier Series:

$$x(t) = \sum_{n=-\infty}^{\infty} c_n \cdot \exp\left(2\pi i \frac{nt}{T}\right). \tag{5.4}$$

In this equation, the c_n determine the strength of the contribution of each sinusoid to the signal and are called the Fourier coefficients, while T/n is its period length. The coefficients c_n can be calculated by integrating the signal $x(t)$, multiplied by the sinusoid of the specific frequency component:

$$c_n = \frac{1}{T} \int_{-T/2}^{T/2} x(t) \cdot \exp\left(-2\pi i \frac{nt}{T}\right) \mathrm{d}t. \tag{5.5}$$

If the signal is a non-periodic function, the frequency spectrum is not a set of discrete values as with periodic signals, but rather continuous. With the Fourier transformation, an arbitrary signal can be expressed by a linear combination of an infinite set of sinusoids. It maps each frequency ω to the amplitude with which its oscillation occurs in the linear combination. The Fourier transformation is referred to as $\hat{x}(\omega)$ and calculated by

$$\hat{x}(\omega) = \int_{-\infty}^{\infty} x(t) \exp(i\omega t) \mathrm{d}t. \tag{5.6}$$

This allows us to study signals not only in the time domain, but also in the frequency domain. However, the calculation above requires signals of infinite length, which can never be achieved in terms of real measurements. Real measurements always have a start and an end. They are sampled with a finite frequency f_s, such that the digital representation of a signal usually is a time-limited, discrete set of data points. In this case, the number of sinusoids needed to represent the signal is also a finite number, which is determined by the number of samples N of which the signal consists. These sets of discrete values can be analyzed using the discrete Fourier transform, a technique to study periodic signals as well as non-periodic ones, which transforms a sequence of measurements x_n, that can be either real or complex, into another set of complex numbers $\hat{x}_k$, which are the complex Fourier coefficients. It is defined by

$$\hat{x}_k = \sum_{n=0}^{N-1} x_n \cdot \exp\left(-2\pi i \frac{kn}{N}\right). \tag{5.7}$$

Algorithms like the Fast Fourier Transform (FFT) are employed to efficiently calculate the expression above. For the FFT, each of the $\hat{x}_k$ values is assigned a frequency, which is determined by the properties of the signal that has been transformed. Having N measurements, sampled at a frequency of f_s, the resolution of the frequency domain is given by

$$\Delta f = \frac{f_s}{N} \tag{5.8}$$

and the maximum frequency that can be extracted from the data is the Nyquist frequency [45]

$$f_{\mathrm{Ny}} = \frac{f_s}{2}. \tag{5.9}$$

This limits the application of the FFT as it has to be made sure that the probed signal of interest lies below a value half of the sampling rate. Furthermore, the resolution of the frequencies that are used in the FFT scales with $1/N$. Therefore, longer traces result in a higher resolution, and the number of samples can be tuned, such that the frequency of interest f is exactly matched by an FFT bin. This condition is met if the ratio between f and Δf is an integer, from which it follows that the number of samples must satisfy the condition

$$N = \frac{k f_s}{f}, \tag{5.10}$$

where N is the number of samples and k must be an integer.

The coefficients $\hat{x}_k$ carry information about the amplitude and the phase of the frequency component. Choosing k to fulfill the condition above allows to extract the phase of the desired frequency, which, in the case of the signals studied in this project, is the beacon frequency. Since each FFT value $\hat{x}_k$ is complex, the phase of a certain frequency, for example, the beacon

frequency, can be extracted from the Fourier coefficients by

$$\phi_k = \tan^{-1}\left(\frac{\mathfrak{Im}(x)}{\mathfrak{Re}(x)}\right). \tag{5.11}$$

With this information, the phase difference between two traces can be determined and from this, with knowledge of the frequency, a time difference can be computed, similarly to the cross correlation. In case of the FFT method, the time difference Δt is given by

$$\Delta t = \frac{\phi_2 - \phi_1}{2\pi f}. \tag{5.12}$$

This method is particularly effective for monofrequent sine waves, such as the beacon signal that has been probed. A single sine appears as a sharp peak in the spectrum of the FFT and is therefore easy to isolate. However, there are limitations on this method as soon as the signal either gets too short, with only a few samples available, and decreasing the resolution of the FFT bins, or if the signal becomes broadband, such that there is no precise frequency at which the FFT peaks, e.g. for a pulsed beacon.

5.3 Digital Band-Pass Filters and Upsampling

For the cross-correlation method, there are two primary factors that limit the ability to determine the time delay with high precision. The first limitation follows directly from the method itself. One can imagine the cross-correlation as a sequence of correlations between two signals, where one signal is shifted against the other by a varying number of samples. However, this shift can only be an integer multiple of the distance between two samples and is therefore directly determined by the sampling rate. Increasing the sampling rate allows for finer steps in the shift of the signal and enables a more precise localization of the maximum of the correlation, which is used to find the time delay.

The second limitation is due to background signals and noise, since cross-correlation is sensitive to features and results in a peak when the same feature appears in both signals. If the feature — in the case of the beacon signal this is the sine wave — is not strong enough to dominate the shape of the trace and noise and background signals have roughly the same amplitude as the signal, it can happen that, by chance, two similar background contributions in two antennas, which are actually uncorrelated, appear as a peak in the correlation stronger than the signal peak or with similar strength. In that case, the cross-correlation will give a wrong value for the time delay.

However, there are methods to increase the sampling rate artificially or to filter unwanted background and noise to purify the beacon signal. Upsampling is a technique to increase the density of samples in the time domain, by manipulating the frequency spectrum of the signal or by inserting zeros in the time domain. Upsampling means that the effective sampling rate is increased. This can be done in two ways. The first way is to take the signal in the time

domain and add a certain number of zeros between each pair of samples. For instance, adding four zeros between each pair of samples corresponds to an upsampling factor of five, since the resampled signal has a length that is five times larger than the original signal. To convert the zeros into values that interpolate the signal, a low-pass filter must be applied to smoothen the signal. Another way to perform upsampling is the modification of the frequency domain. In this method, the signal is first transformed by an FFT to access the spectrum. Then, a zero padding is performed in the frequency domain, where a block of zeros is inserted between the positive and the negative frequencies of the FFT. After the insertion, the FFT is inverted to get back to the time domain, where the signal is now denser than before. This method is a computationally cheap and fast method to increase the effective sampling rate of a signal using offline analysis techniques. It has been used in the studies of the beacon signal.

To address the limitation caused by noise in the recorded traces, digital filters can be applied to the signal. The basic idea is to only pass a specific part of the spectrum, while the other frequencies are suppressed. For the beacon signal analysis, a Butterworth filter was chosen [46]. Its properties are such that the filter has a flat shape in the pass band with no ripples. The band-pass filter removes unwanted RFI, like that coming from commercial radio transmitters or other sources that disturb the beacon signal. These two restrictions only apply to the cross-correlation method and do not need to be used in analyses with the FFT technique.

CHAPTER 6

Measurements of the Time Synchronization with Three Antennas

The test system has been developed in several stages. Therefore, three measurement campaigns have been conducted, testing the synchronization of the beacon signal with different setups. In between the campaigns, the test system was updated, and a series of tests was initially carried out in the lab to ensure functionality of the hardware and to show that the analysis methods deliver the expected results. The test system has been designed to not be installed permanently at a specific location, but can be assembled and disassembled within approximately an hour. What all three measurement campaigns have in common is that the data was stored on a laptop and analyzed offline after the measurement was finished, using the techniques described in Chapter 5. Furthermore, the three campaigns took place at the same location. To be mostly undisturbed by buildings or other types of infrastructure that could influence, for instance, the path of the beacon signals, we chose a large open field, the Panzerwiese (50.88708° N, 8.01639° E), not far from the Emmy-Noether-Campus of the University. The site is located next to a path, allowing access with the equipment required for the test system. The location is situated on a hill, ensuring the best possible view for the antennas. Since there is no infrastructure in the surrounding area, and to adapt the conditions to those at Auger, the test system was supplied autonomously with a local energy source. There is a parking lot at the foot of the hill, to which the test system was brought with several cars. From there, it was transported with the help of a handcart to the position where the antennas and DAQ electronics were set up.

In the first measurement campaign, which took place in November 2024, the beacon signal was recorded using a digital oscilloscope, which has been described previously in Chapter 4. On the one hand, the oscilloscope offers the advantage of live observation of the signal on its screen. Issues like a wrongly connected antenna or problems with the beacon were immediately apparent and could be fixed. However, using the oscilloscope also has a disadvantage. The antennas must be rather close to each other and to the oscilloscope, since they must be connected via a signal transmission line, which in that case was a coaxial

cable. This limits the spacing between the antennas, and distances in the order of 100 m or more, as occur in AERA, cannot be achieved in this arrangement. The second measurement campaign took place in June 2025, followed by another one in September 2025. A few things were done differently compared to the first measurement. Besides the readout system, which has been changed from oscilloscope-based to AERA digitizers, the power supply has been changed and is no longer central to the DAQ system. Instead, each station had its own supply driven by a battery. In this setup, the only physical connection between the antennas was the optical fiber that connected the WR stations. This setup is the closest to the setup at Auger in Malargüe. However, due to the limited length of the available fiber and the landscape conditions in Siegen, a baseline at the order of km range could not be reached in these tests.

6.1 Measurement with an Oscilloscope

In November 2024, we conducted the first measurement campaign at the local field. In this test, three butterfly antennas were placed in an approximately equilateral grid with a baseline of about 25 m. A central DAQ station was set up, close to the antenna, which was the nearest to the beacon. At the DAQ station, there was a 4 GSa/s oscilloscope, a signal generator for the beacon, and a laptop to collect the data from the oscilloscope. All three devices must be running on a 230 V supply. This was provided by a gasoline generator, which was placed about 52 m away from the devices to reduce the noise coming from this device. It had been tested at the campus of the University that the influence of the gasoline generator on the signal was minimal. At the DAQ station, there was a power strip to supply up to 6 devices at the same time. The antennas were connected to the supply board, which provides the power for the LNAs and separates the RF signal from the DC part. From there, the *signal out* port of each board was connected to one of the channels of the oscilloscope with a BNC cable, 2 m in length. The antennas were connected with 30 m BNC cables to the DAQ station. The length of these cables was the main limitation in terms of spatial distance between the antennas and determined the baseline of the measurement. The beacon antenna was also connected with such a cable, and was placed in the opposite direction of the DAQ station with respect to the receivers. This created a maximum distance of about 50 m between the beacon and the receiver that was the furthest away from it. To avoid confusing the antennas in the data analysis, they were numbered from 1 to 3 and recorded with the corresponding channel number on the oscilloscope. In Figure 6.1, the positions of the beacon and the receiving antennas along with their distances are shown. Furthermore, the position of the DAQ station and the generator are marked on the map. Figure 6.2 shows the DAQ setup, i.e. the oscilloscope and the laptop, and two of the receiver antennas. The electronics were placed on portable folding tables to protect them against moisture on the ground. A beacon frequency of 64 MHz was chosen in this test. This value lies within the frequency band used by the AERA beacon.

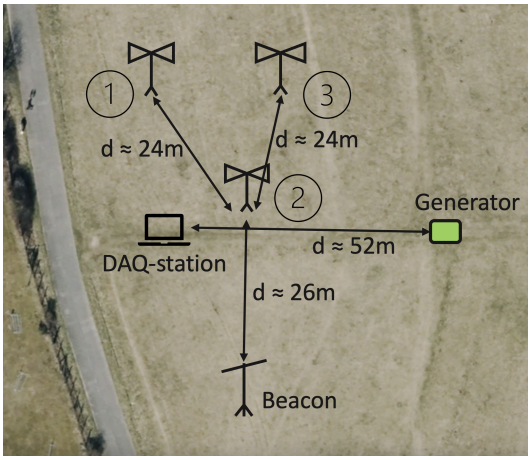

Figure 6.1: A map that indicates the positions of the antennas in the test field. The antennas are numbered to distinguish them in the data analysis. A gasoline generator was taken for the power supply and was placed as far as possible from the rest of the electronics.

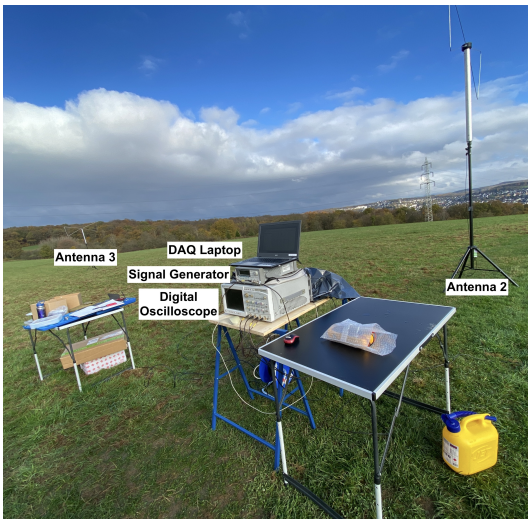

Figure 6.2: Setup for the first beacon measurement. Antennas were read out using a 4 GSa/s oscilloscope and the data was saved on a laptop.

Recordings of the beacon signal were made at different amplitudes varying between 1 V_{pp} and 8 V_{pp}, which have been adjusted at the signal generator. The idea was to simulate different distances between the beacon and the other antennas, as the length of the BNC cable limited the physical distance. Each recorded trace has a length of 32 000 samples, corresponding to 8 µs of data at a sampling rate of 4 GSa/s. The size of a correesponding file is around 2 MB. The number of recorded events — an event referres to a reaout of at least one channel of the oscilloscope, but can also include multiple channels — was chosen randomly and varied between 150 and 330, since the readout software does not offer a parameter to fix the number of events to record. A recording must always be manually started and ended by the user. No analog filter was applied to the data before the recording, unlike in the AERA digitizers. Therefore, background signal outside the 30 MHz to 80 MHz band is recorded alongside the beacon signal, which makes a cross-correlation analysis on the raw data quite challenging. To tackle this issue, a digital band-pass filter with a lower cutoff of 30 MHz and an upper cutoff of 70 MHz has been applied to the data prior to the timing analysis. The reason why the upper cutoff frequency was set at 70 MHz is that there is a strong RFI source at 88 MHz coming from a local radio station. Figure 6.3(a) shows the average power spectrum of antenna 1, one of the two that is further away from the beacon. The blue curve represents the raw spectrum, without any data processing. There is a sharp peak at 64 MHz, which is the beacon frequency, and two more peaks, not as sharp, but with approximately the same strength. One of them is the local radio station, mentioned before, and the other one is also a radio broadcaster, transmitting at a frequency of 105.7 MHz. Furthermore, there is some

broadband noise between 10 MHz and 30 MHz whose origin is not understood. Comparing the blue curve with the orange one, where the band-pass filter has been applied, it can be seen that most of the background signals, especially the RFI below 25 MHz and above 90 MHz, are strongly reduced. Also the sharp peak at 88 MHz is now suppressed by approximately 40 dB. This effect can also be seen in Figure 6.3(b). The top plot shows the raw signals for each antenna, which look chaotic as it is a superposition of many frequency components. With the cross-correlation method, it would be very difficult to extract any information from these curves. In the lower plot, on the other hand, the signal has been passed through the filter. The feature of the beacon signal is clearly visible, and cross-correlation can be applied to this signal.

To measure the timing of the beacon signal, the cross-correlation and the FFT method described above have been applied to the data recorded in this measurement. In principle, it is expected that both methods would deliver the same results. The idea of using the two methods is to cross-check and validate one with the other. As it is done for the beacon analysis in AERA, one antenna was chosen as a reference station, and the other two were compared to that one. In the case of this measurement, antenna 1 serves as the reference, and the phase difference or time difference (note that there is just a conversion factor of $1/2\pi f$ between those values) has been determined. In the case of the cross-correlation analysis, upsampling with a factor of 10 has been applied to the signal to effectively increase the sampling rate from 4 GSa/s to 40 GSa/s. Furthermore, both signals were passed through a band-pass filter before being analyzed for timing. For the FFT analysis, this should not make any difference, since the beacon is investigated in the frequency domain, and the strength and phase of the beacon frequency stay untouched by the filter. The time delay has been measured between antenna 1 and 2 and between antenna 1 and 3. The results are shown in Figures 6.4 and 6.5. In this measurement, sub-nanosecond precision stability has been achieved between the two pairs of antennas. More precisely, the uncertainty was determined to be about 115 ps. The histogram shows a structure as if two distinct ranges of values were measured, each with a sub-distribution. This artefact is likely related to the sampling rate of the oscilloscope. The distance between the two distributions corresponds exactly to the distance between two samples at 4ĠSa/s. This leads to the assumption that, despite upsampling, the resolution is mainly determined by the recording hardware.

The same measurement has also been done for a set of other beacon amplitudes between $2\,V_{pp}$ and $8\,V_{pp}$ and their results are summarized in Figures 6.6 and 6.7. It can be seen that all results agree well within 30 ps and the spread of the distributions is similar for all measurements and reaches sub-ns precision.

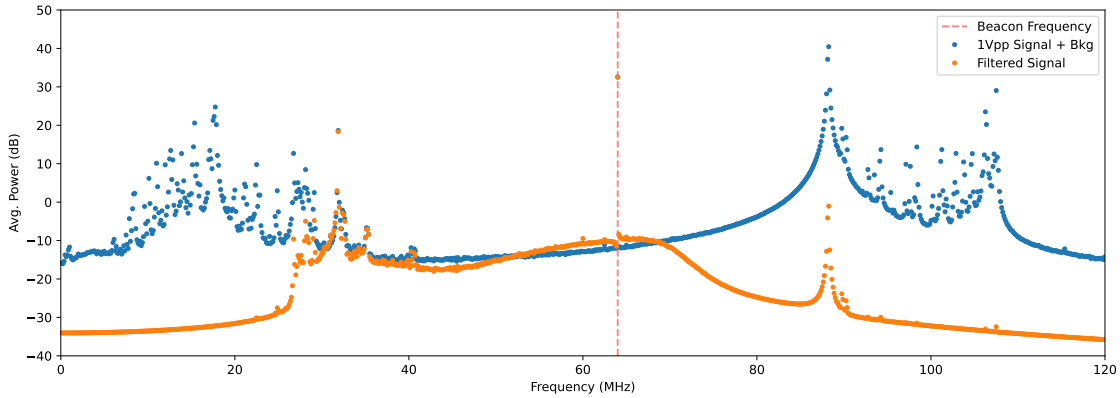

(a) Average power spectrum data recorded with the oscilloscope at the beacon test. The beacon frequency of 64 MHz is marked by the dashed line. Other strong peaks appear in the raw signal (blue) at 88 MHz and 105.7 MHz, coming from commercial radio stations. In the filtered signal (orange), RFI from neighboring bands are suppressed.

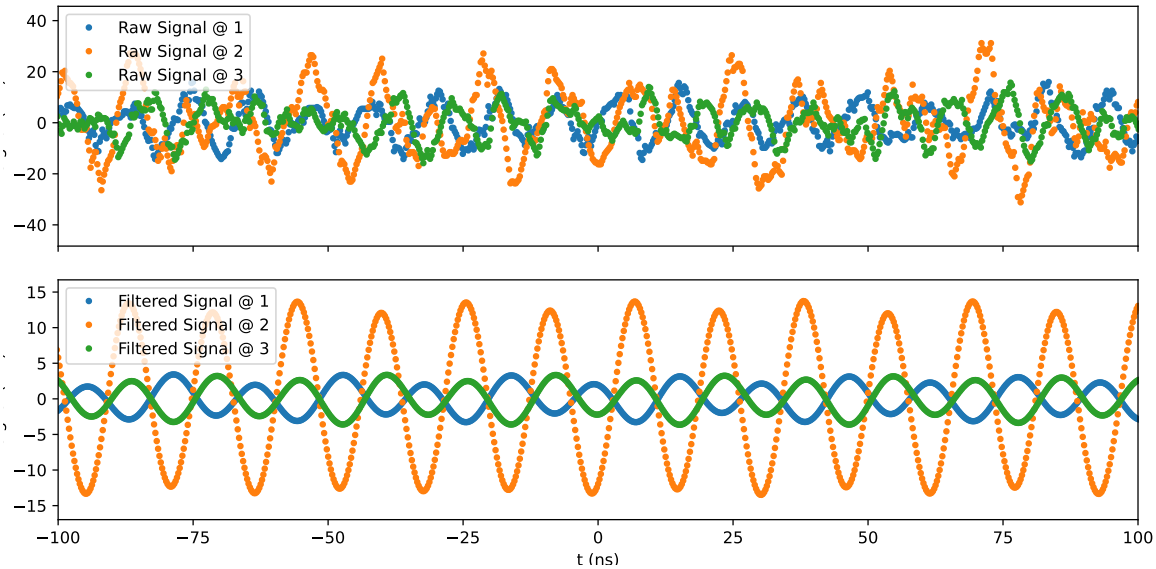

(b) Typical traces recorded by the oscilloscope on channels 1 (blue), 2 (orange) and 3 (green). The channel configuration has been chosen to match the numbering of the antennas in Figure 6.1. After applying the band-pass filter, the beacon signal becomes visible and one can see the phase difference between the antennas, which is not the case for the raw signal. Antenna 2 is closer to the beacon and hence records a stronger beacon signal.

Figure 6.3: Oscilloscope measurements at the beacon test: (a) power spectrum before and after filtering, (b) example time-domain trace before and after filtering.

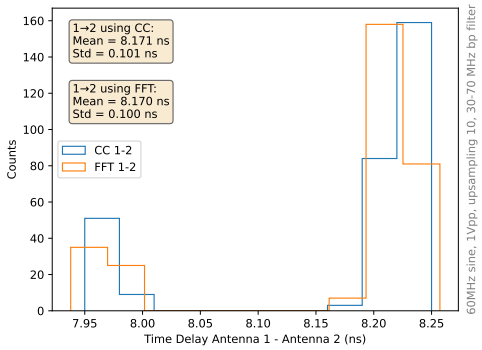

Figure 6.4: Relative time delay between antenna 1 and 2 measured using cross-correlation (blue) and Fourier transform (orange). The key value is the width (Std) of the distribution, as it measures the beacon synchronization ability. Both methods agree well and a sub-ns precision has been reached in this test.

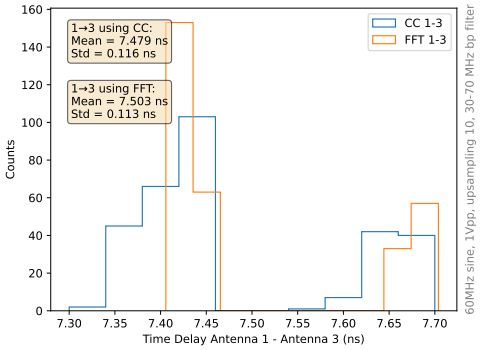

Figure 6.5: Relative time delay between antenna 1 and 3 measured using cross-correlation (blue) and Fourier transform (orange). The key value is the width (Std) of the distribution, as it measures the beacon synchronization ability. Both methods agree well and a sub-ns precision has been reached in this test.

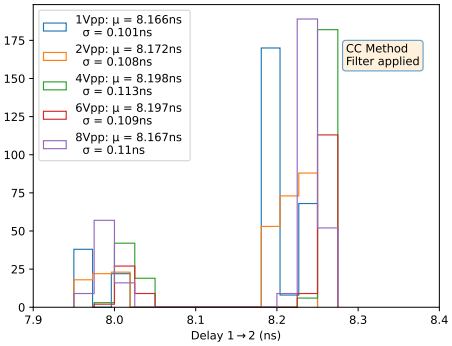

Figure 6.6: Overlay of histograms showing the time delay between antenna 1 and 2, measured using cross-correlation (CC). The means and standard deviations are shown as well. Different colors correspond to different amplitudes between 1 V_{pp} and 8 V_{pp} at which the beacon was operated.

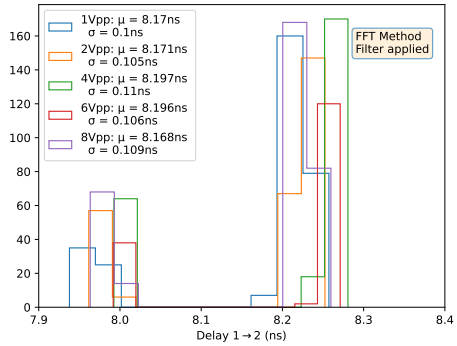

Figure 6.7: Overlay of histograms showing the time delay between antenna 1 and 2, measured using Fourier transform (FFT). The means and standard deviations are shown as well. Different colors correspond to different amplitudes between 1 V_{pp} and 8 V_{pp} at which the beacon was operated.

6.2 Measurement with AERA Digitizers and WR PPS

For the further development of the test system, the readout electronics were modified from a single oscilloscope to a set of 3 AERA digitizers. The primary reason for the change is that transporting heavy oscilloscopes to the field in Argentina is a challenging task. Furthermore, employing AERA hardware is much closer to the conditions at Auger, and the hardware is cheaper and more readily available. At this stage, the WR hardware has also been implemented in the test system. The original plan was to use the PPS signal from WR as an external trigger source for a set of three oscilloscopes. However, it can also be used to supply AERA digitizers with a PPS. Some modifications that were made to provide an external PPS to a digitizer have been described in Chapter 4 and included an additional PCB mounted between the digitizer board and the GPS board. With the new setup, the readout of the butterfly antennas takes no longer place at a central DAQ station, but rather individually at each station. Three stations were used to record the beacon signal in three different positions, each with its own name, which is formed from the serial number of the digitizer. The digitizers used in the test system are AERASN301, AERASN336, and AERASN344. A second measurement campaign was conducted at the same location as the first one. Compared to the previous setup, the antennas were placed at larger distances of approximately 100 m, which is at least of the same order of magnitude as the smallest antenna distances at AERA (150 m for phase 1 antennas). At the central location, where the oscilloscope was previously situated, a laptop was collecting data from all three antennas, which were connected to the digitizers via the WR network. In Figure 6.8, a map of the distribution of the antennas is shown, including the distances between the stations and the beacon's position.

Delocating the DAQ, however, comes with a new challenge. While previously a centrally located generator powered all antennas, each station must now have its own power supply, as using long extension cables is impractical. For this purpose, a set of 4 battery-driven power stations has been used to supply both the readout electronics, including WR, and the signal generator to power the beacon. This change also made it possible to place the beacon at an arbitrary position that is no longer connected to the central station via a cable, as was the case in the first beacon measurement. The power stations used in this setup have a capacity of 300 Wh and can deliver a variety of output voltages, including 5 V DC, 12 V DC, and even 230 V AC. Thus, the DC outputs deliver exactly the voltages required to operate the test system. The WR LEN modules are powered from the 5 V USB port, while the digitizers are connected to the 12 V barrel jack connector, which has a size of 2.1 mm. The 230 V AC output has been used to power the signal generator for the beacon. The power consumption of each station is displayed on the power station's screen. It typically falls within the range of 10 W to 20 W, depending on whether the digitizer is actively streaming data or not. This allows multiple hours of data taking without interruptions. However, the signal generator for the beacon consumes significantly more power and therefore represents the most significant limitation on the duration of the measurement campaign. Overall, a measurement duration of more than 4 h was possible. To extend the duration of a measurement, it is in principle possible to plug a solar panel into the power station and provide additional power that can

even charge the battery if more power is generated by the solar panel than consumed by the test system, but in practice, this was not needed for the tests that were performed.

Since the test took place in a field, the digitizers and WR stations were protected against moisture by placing them on a plastic plate. The antennas were connected to the first high-gain channel of the digitizer via a 15 m BNC cable, and the PPS from the WR was hooked up to the external input on the front panel. An example of one of the stations can be found in Figure 6.9. It shows the setup at station 301, which is the closest to the laptop from which the readout is done. The laptop and the switch are connected with a 10 m Ethernet cable, whereas all WR-LENs are connected with short Ethernet cables to the digitizers. The WR network has been set up such that the master was at one of the remote stations and the first slave, which forwards the WR link to the second one, was located at the nearest station with respect to the position of the laptop. This comes with the advantage that the fiber spools can be placed close to the central position, making the assembly of the test system easier. Connecting the laptop to any of the other WR LENs would have worked too.

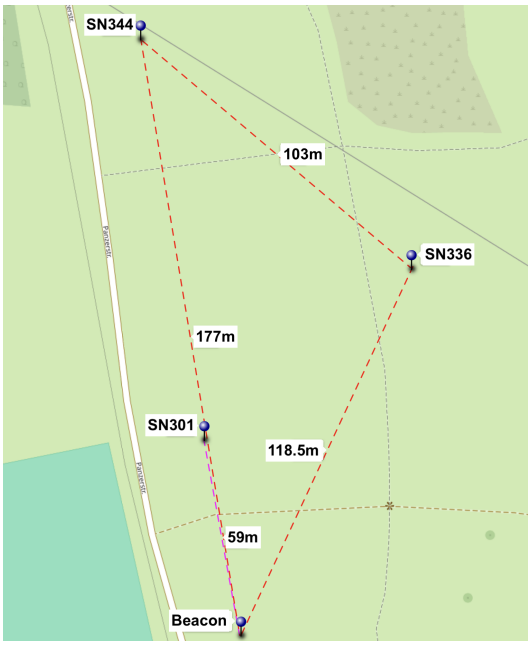

Figure 6.8: Map showing the positions of the three stations (antennas connected to AERA digitizers) and the beacon position. The distances between the positions are also indicated.

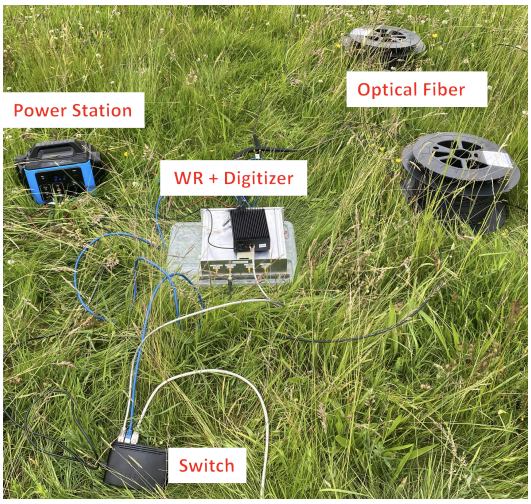

Figure 6.9: Setup for power and DAQ at station 301. From here, the optical fiber is distributed to the two other stations and a network switch connects the WR LEN and the digitizer to the laptop.

Before moving the test system to the field, the new DAQ method and the functionality of the parallel readout of three digitizers were tested in the lab to ensure that the system runs without complications. The same applies to the power supply of the stations with batteries. Additionally, during the campaign, where everything was moved to the field and set up as

described above, a communication check was conducted by pinging each station with its fixed IP address and establishing a Telnet connection with all digitizers. For the beacon measurement using the oscilloscope, the signals can be monitored live on the device's screen. This, however, is no longer possible with readouts using digitizers. Therefore, a rapid analysis pipeline was developed, which takes the latest event from each station, decodes its raw data into a text file, and plots a portion of each trace, as well as the FFT from the signals. This offers the opportunity to monitor the beacon signal by checking the spectrum and seeing if the beacon line is present. The digitizers have an integrated band-pass filter and an internal gain, which already suppresses most of the background signals observed in the measurement with the oscilloscope. Another main difference is that the sampling rate is only about 5% of that of the scope. This means that only about three samples are recorded per period of the beacon signal. On the other hand, the traces taken with the digitizer were much longer; to be precise, each trace consisted of 20 480 samples, which corresponds to a trace length of 1.1 ms. This is 10 times longer than the usual traces taken at AERA, but it has the advantage that the resolution in the FFT spectrum is increased.

Measurements were taken at a beacon amplitude of 2 V_{pp}, which turned out to be a sufficient value to clearly see the beacon in all three antennas but not saturating the ADCs in the antenna closest to the beacon. In contrast to the first measurement, different beacon frequencies were tested. The first measurement was performed with a beacon frequency of 60 MHz, because it was also used for some lab measurements and divides conveniently the 180 MHz sampling rate nicely. In the second measurement, the frequency was tuned to 58.887 MHz, one of the frequencies used at AERA. The readout system allows setting a fixed number of events that should be read out. In order to obtain a sufficiently large sample, the number of events was set to 500 in each case. For each event, three files were generated, one from each antenna, which were analyzed offline using the same methods employed in the oscilloscope measurement campaign.

The average power spectrum of the data is shown in Figure 6.10. There are significant differences in the shape of the spectrum compared to the one from the first campaign. One can see the structure of the band-pass filter, with a strong peak within the passband at 60 MHz. This peak is the beacon line, and it is the strongest signal registered by the antennas. The second-strongest signal is the already known radio transmitter at 88 MHz. According to the Nyquist–Shannon sampling theorem [45], the sampling rate must be at least twice as large as the largest frequency that is investigated. Therefore, the spectrum is cut at 90 MHz, which is half of the sampling rate of the digitizers. The noisy band around 30 MHz, on the other hand, is still within the data. Furthermore, a new narrow peak appears at a frequency of 50 MHz. The origin of this peak is unknown, and its source must be either distant or very weak. In any case, it does not interfere with the analysis of the data.

The results from the timing analysis, which has been performed on both datasets, show a worse result compared to the previous measurement. Even though both methods, cross-correlation and FFT, agree well again, the overall accuracy did not reach the sub-ns level in this analysis. This can be seen in Figures 6.11 and 6.12, where the histograms of the time delay between each combination of antennas are shown. Based on this observation, a

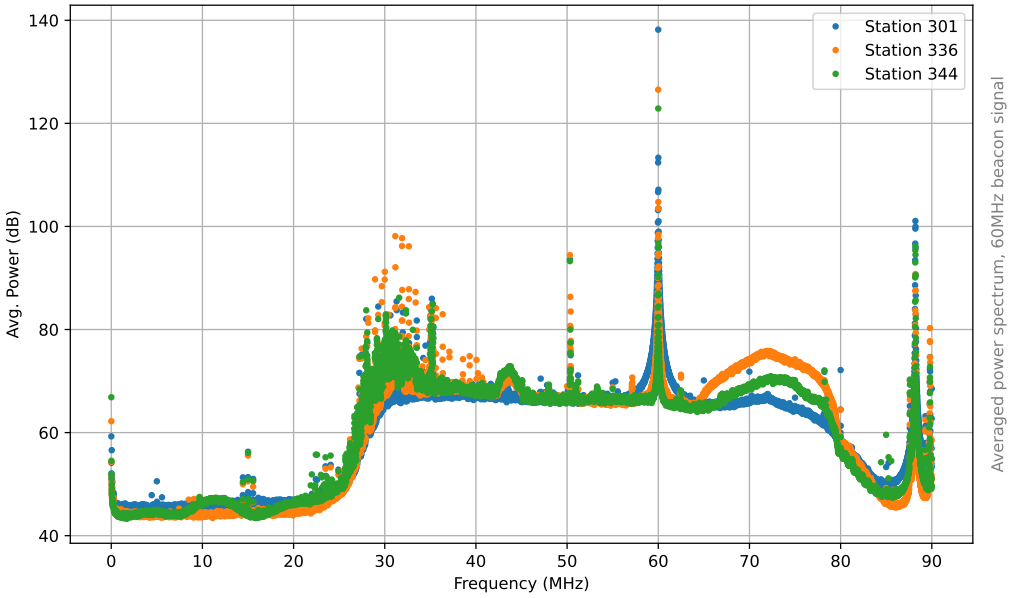

Figure 6.10: Average power spectrum of the data recorded with the stations 301 (blue), 336 (orange), and 344 (green) at different locations. The 30 MHz to 80 MHz band-pass structure is clearly visible, and the beacon line stands out at 60 MHz. Further narrowband transmitters at 50 MHz and 88 MHz are suppressed compared to the beacon. Broadband RFI was observed around 30 MHz, but did not affect the analysis.

measurement in the lab was conducted, where two digitizers were hooked up to the signal generator with cables of equal length. Then, the generator signal was recorded in both stations, and with the cross-correlation analysis, the same spread of the time delay was confirmed. The standard deviation of all these measurements is between 2 ns and 3 ns. Figure 6.13 shows a section of a set of six consecutive traces recorded in the field with the 60 MHz beacon. Assuming that the propagation time of the beacon signal from the transmitter to the receiver is determined by the geometrical distance, a fixed and stable phase difference between two receivers is expected. A comparison of the signals, however, shows that the relative phase between station 336 and station 344 drifts from event to event by several nanoseconds. The same drift was observed for the other pairs of stations. This behavior leads to the conclusion that there must be clock drifts within the digitizers that are not related to the PPS, where the precision is known to be in the sub-ns range from measurements in the lab, but must have another source, which cannot be resolved by the WR. The value of the spread indicates that there is a clock drift of up to ±1 sample for each digitizer.

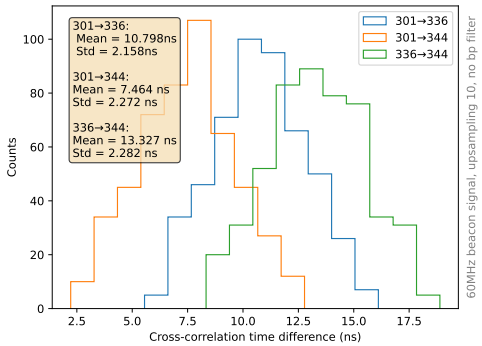

Figure 6.11: Signal time delay between stations 301 and 336 (blue), 301 and 344 (orange), and 336 and 344 (green) for the 60 MHz dataset recorded in the field and analyzed using the cross-correlation method. The standard deviations of the distributions are below 2.3 ns.

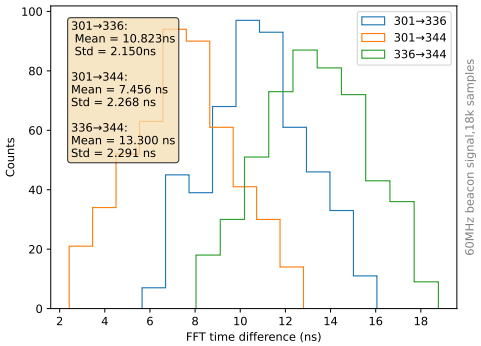

Figure 6.12: Signal time delay between stations 301 and 336 (blue), 301 and 344 (orange), and 336 and 344 (green) for the 60 MHz dataset recorded in the field and analyzed using the FFT method. The standard deviations of the distributions are below 2.3 ns.

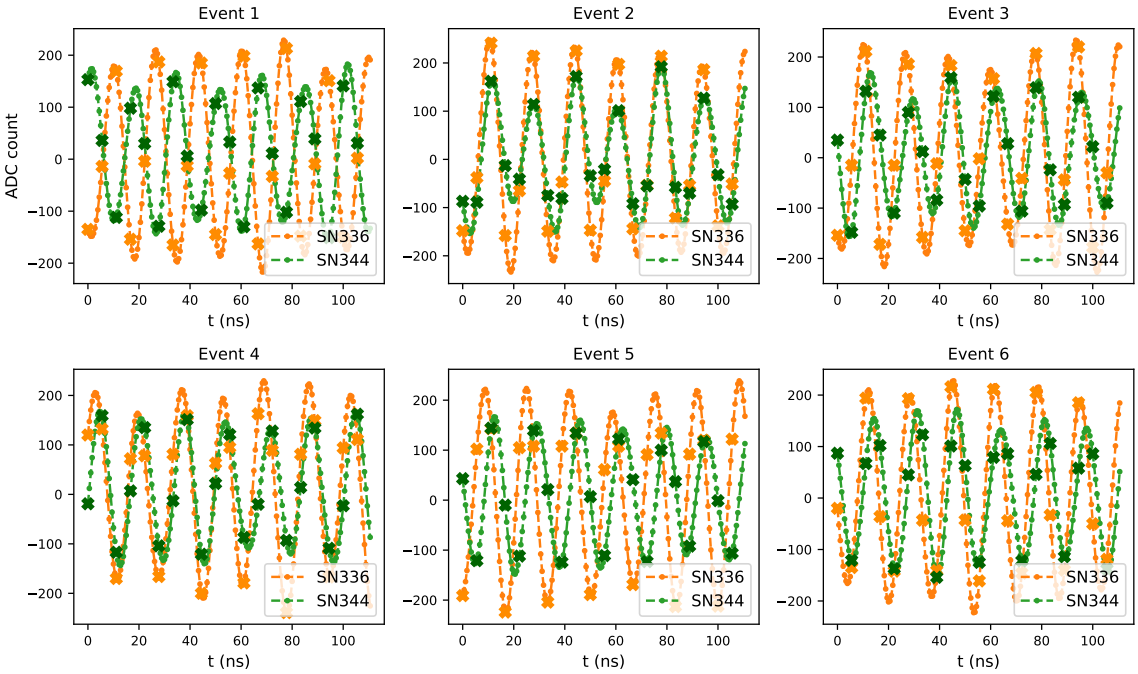

Figure 6.13: Excerpts of the signals in stations 336 and 344 for consecutive events. The phase difference between the signals varies significantly from event to event indicating internal clock drifts.

6.3 Measurement with AERA Digitizers, WR PPS and 10 MHz Clock

Based on the results of the previous measurement in June 2025 with the digitizers at the Panzerwiese, which showed that the synchronous PPS signal alone is insufficient to achieve sub-ns synchronization, a method was developed to correct the delays, which were presumably internal. The idea behind the correction method is that the time difference between two antennas consists of two components: the phase difference of the beacon signal, and the internal delays, which vary for each digitizer. Only the sum of both can be measured. The total delay can be expressed as

$$\Delta t_{\text{meas}} = \Delta t_{\text{beacon}} + \Delta t_{\text{internal}}, \tag{6.1}$$

where Δt_{beacon} is the value that is important to study the beacon performance, and $\Delta t_{\text{internal}}$ comes from parasitic effects. These internal delays can be corrected with the help of an additional synchronous signal provided by WR. Besides a PPS signal, it also provides a synchronous 10 MHz clock, which was attempted to be used for these corrections. In a third measurement campaign, the test system was set up in the same location as for the second one, where the digitizer readout was used for the first time. But, in contrast to the previous measurement, the 10 MHz clock of the WR was also recorded at one of the available analog inputs of the digitizer. However, it was not possible to connect the WR clock with the digitizers that are equipped with a filterboard for AERA V3 digitizer without modifying the signal, because the amplitude of the clock, which is ±1 V, exceeds the dynamic input range of the ADCs, even when it is hooked up to the low-gain channel. To adjust the signal such that it is compatible with the maximum input levels of the ADCs, a 20 dB attenuator was connected between the clock output and the digitizer input, in case it is a filterboard for AERA V3 digitizer, since there is a difference in the amplification between filterboards for a V2 and V3 digitizer. Still, with the attenuator included, the signal was too strong; however, since it occurred equally on all devices, the patterns recorded were the same at all stations. Furthermore, a DC voltage is present at the analog input to supply the LNAs, which could affect the clock output of the WR-LEN. This DC voltage was blocked by placing a capacitor in series with the 10 MHz clock. However, due to the presence of the filter board, the clock signals were no longer rectangular but appeared as a periodic, damped oscillation.

With the extended setup, three sets of data were recorded, in each of which a different beacon frequency, namely 58.887 MHz, 68.555 MHz, and 71.191 MHz, was tested. This time, the evaluation of the beacon phase was performed using the FFT method only, as it was previously demonstrated that cross-correlation and FFT yield the same results. In addition, the delay of the WR clock signal has also been measured for each event individually; however, since a square wave is a superposition of many sinusoidal frequencies, an FFT analysis is not suitable in this case. Therefore, cross-correlation in combination with upsampling has been used to measure the delay between the clocks. Preliminary measurements in the lab have shown that the offset between 10 MHz clocks of two WR stations varies only within a range of a few picoseconds. These results show that the WR clock is a reliable source for the offline synchronization.

When analyzing the data recorded with the beacon operating at 71.191 MHz, the first step was to calculate the delay for the beacon signal and the WR signal, individually. In the next step, the WR offset was subtracted from the beacon delay to account for the internal effects. Ideally, this should provide a value close to the actual beacon phase or time difference. The method has shown a significant improvement for at least one of the datasets analyzed in this constellation. Figure 6.14 shows the delay between the 10 MHz signals when pairs of antennas are compared. The width of the distributions is a further indication of the ±1 sample offset that can occur during data acquisition. These offsets were used to correct the beacon delay. The results of the beacon measurement before and after the correction can be found in Figure 6.15. It can be seen that with the correction, the width of the distribution shrank below the nanosecond range, indicating that, at least on the scales tested in the campaign, the beacon signal can be used for sufficient synchronization.

A second dataset, where the beacon was transmitting at 58.887 MHz, shows a similar result for at least one pair of antennas, SN336 and SN344. The other pairs have a larger value of σ, which is mostly determined by some outliers that are still off by -1 sample, even though a correction was applied. It seems that in these cases, the correction was not working properly. Such outliers could be identified in further analysis and be removed or corrected. Overall, however, the performance remains in the sub-ns range, with a spread between 300 ps and 400 ps. This can be seen in Figure 6.16. The same analysis was also applied to the 68.555 MHz dataset, but it did not yield the expected results this time. In this case, the distributions of the beacon signal delay without the correction being applied looked similar to the ones from the other two measurements. However, the correction signal itself exhibited unusual behavior. The delay between the WR clocks showed no longer a distribution with a width of approximately 2.5 ns as it was the case before, but has taken values in the range from −500 ns to 500 ns in all combinations of digitizers. The reason for this has not yet been determined, and the data have not been taken into account for further analysis.

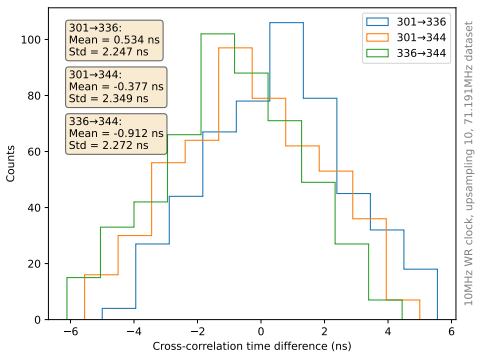

Figure 6.14: Measurement of the delay of the WR 10 MHz clocks recorded with AERA digitizers. The delay has been measured between station 301 and 336 (blue), 301 and 344 (orange) and 336 and 344 (green) using cross-correlation. The mean values are smaller than 1 ns, and the standard deviations are in the ns range. Even though the signal should be synchronized, a varying offset between the stations has been calculated and subtracted from the beacon time difference.

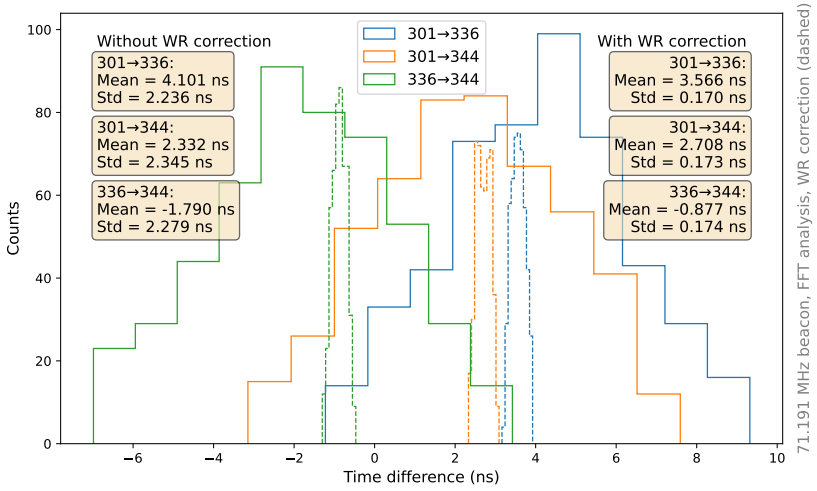

Figure 6.15: Result from the measurement of the beacon synchronization at 71.191 MHz before and after applying the WR correction. The solid line represents the uncorrected time delay between the stations 301 and 336 (blue), 301 and 344 (orange), and 336 and 344 (green), while the dashed lines show the delay after subtracting the WR clock offset, using the same color coding. Subtracting the offset reduces the width of the distribution to the sub-ns range.

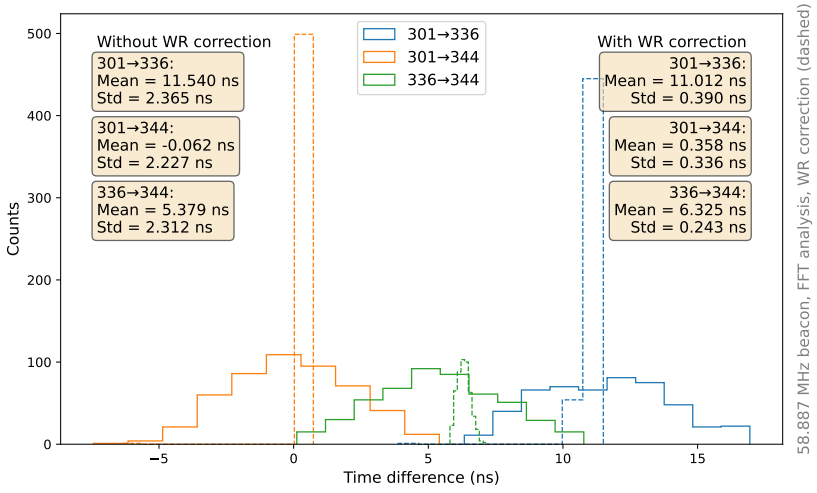

Figure 6.16: Plot corresponding to the one above, but for a beacon frequency of 58.887 MHz. After applying the WR correction, the standard deviations of the distributions are reduced to the sub-ns level. The delays between 301 and 336, and between 301 and 344 include outliers that are off by -1 sample, leading to standard deviations that are increased by approximately 100 ps to 150 ps.

CHAPTER 7

Summary and Outlook

Modern techniques use interferometry to study cosmic rays by observing their radio emissions with an array of ground-based antennas. These techniques are becoming more and more popular as they enable the reconstruction of X_{max}. Interferometric methods, in particular, rely on precise time synchronization at the sub-nanosecond level. At AERA, an extension of Auger to perform detection of cosmic ray-induced air showers with radio antennas, a combination of GPS-based timing and a reference beacon is used to synchronize the detector. The beacon transmits continuous radio signals to supply the AERA stations with a reference signal. This signal is used in offline analysis to correct GPS timing drifts, which can reach several tens of nanoseconds. During calibration measurements using airplane signals to correct for these drifts, a timing accuracy of about 2 ns was demonstrated, indicating the potential to reach sub-ns precision.

In this thesis, a test system has been developed to verify the synchronization method based on GPS timing in combination with a beacon correction. The test system is designed to record the beacon signal at three radio antennas, synchronized externally using clock signals disciplined by a WR network. For the readout of the antennas, an oscilloscope with four channels, and later a set of three AERA digitizers, has been used. The digitizers were modified by inserting a PCB that allows selecting between a PPS generated from the GPS board or from an external source. This modification was necessary to enable the integration of the WR network with the AERA digitizers. At each station, there is also a WR-LEN, which provides the PPS signal and a 10 MHz clock to the digitizer. Initial tests of the beacon synchronization were conducted using a single oscilloscope. This method has the disadvantage that the antennas must be read out by a single device at a central place, requiring coaxial cable connections between the antennas and the oscilloscope. The necessity of cables leads to a limited range of distance between the antennas. With the switch to a readout based on AERA digitizers, the DAQ electronics was distributed, similarly to the configuration of large-scale cosmic ray radio detector arrays, and data was transferred via a 250 m single-mode fiber to a laptop, from which the readout was controlled.

Three measurement campaigns were carried out during the course of the work, during which the test system was adjusted accordingly. In the first campaign, the antennas were read out by the oscilloscope and hence their distance reached only up to 25 m. In this setup, the WR system was not needed since the data was collected locally with a single device. After this test, the readout has been switched to the modified digitizers, and multiple tests to check the functionality of the new readout method were conducted in the lab, before moving the test system to the field again. In the second and third campaigns, WR was also included, and the distance between the antennas increased to the order of 100 m, which is closer to the distances of antennas at AERA, but still an order of magnitude smaller than the distance between two antennas at RD. These campaigns serve as a proof of principle. The range of the test system can be expanded by using longer optical fibers and a geographical condition with a sufficiently wide field of view.

The recorded beacon signal has been analyzed using signal processing techniques like cross-correlation and FFT. With these methods, the phase or time delay between antennas has been determined, and its stability investigated. In the cross-correlation analysis, which searches for identical features in the signals, a digital band-pass filter was applied to suppress the background from commercial radio stations. The results from the cross-correlation and the FFT analysis were consistent. The oscilloscope-based measurements determined a stability of the beacon synchronization of about 120 ps, meeting the sub-ns requirements mentioned above. This result was obtained at short baselines, and in the first measurement with the digitizers, the synchronization was less precise. In this measurement, the stability of the beacon signal could only be determined within 2.5 ns. Presumably, the cause of the degradation lies in the drifts of the digitizers' clocks. This effect was then reduced by employing the 10 MHz clock signal from the WR network recorded simultaneously with the beacon signal. The clock signal is known to be synchronized, based on stability measurements of the WR system using a fast oscilloscope. To this end, the drifts between digitizers were measured and corrected in the following offline analysis. Applying this correction allowed a beacon signal stability verification better than 400 ps.

The test system showed that synchronization of autonomous radio antennas using a beacon is possible on short baselines, but to measure it with sufficient precision, offline corrections from external clock signals are needed. Further plans include installing the test system at the Auger site and increasing the scale in sequential steps up to km distances. A good starting point for this would be three AERA stations, close to the CRS, which are already equipped with an optical fiber. Later, it could also be moved to other places within the observatory, but this requires more effort as existing infrastructure cannot be utilized, and hence, long fiber cables must be laid. Another test, that could be performed beforehand, is to only use the 10 MHz clock on the ADC input to apply the correction and switch back to GPS for the PPS source. If this works, no modification of the digitizers would be necessary, and existing hardware from Argentina could be used in the field. However, wireless synchronization of autonomous detectors remains a challenging task because there is no central timing source, and the propagation effects of the synchronization signals are not precisely known.

Bibliography

[1] Nobel Prize Outreach, *The Nobel Prize in Physics 1936*, https://www.nobelprize.org/prizes/physics/1936/summary/, Accessed: 2025-08-11, 2025.

[2] D. J. Bird et al., *Detection of a cosmic ray with measured energy well beyond the expected spectral cutoff due to cosmic microwave radiation*, The Astrophysical Journal **441** (1995) 144.

[3] M. Tanabashi et al., *Particle Data Group*, Physical Review D **98** (2018) 030001.

[4] P. Picozza et al., *PAMELA–A payload for antimatter matter exploration and light-nuclei astrophysics*, Astroparticle Physics **27** (2007) 296.

[5] K. Greisen, *End to the cosmic-ray spectrum?*, Physical Review Letters **16** (1966) 748.

[6] G. T. Zatsepin and V. A. Kuz'min, *Upper limit of the spectrum of cosmic rays*, Journal of Experimental and Theoretical Physics Letters **4** (1966) 78.

[7] F. Camilo et al., *Discovery of two high magnetic field radio pulsars*, The Astrophysical Journal **541** (2000) 367.

[8] A. M. Hillas, *The origin of ultra-high-energy cosmic rays*, Annual Review of Astronomy and Astrophysics **22** (1984) 425.

[9] T. Stanev, "Cosmic Rays in the Atmosphere", *High Energy Cosmic Rays*, Springer International Publishing, 2021.

[10] K.-H. Kampert and M. Unger, *Measurements of the cosmic ray composition with air shower experiments*, Astroparticle Physics **35** (2012) 660.

[11] *Cosmo Cascade*, 2014, URL: https://www.antarcticglaciers.org/wp-content/uploads/2014/11/cosmo-cascade.png (visited on 14/08/2025).

[12] J. Linsley, "Standard value for the radiation length in air", *19th Intern. Cosmic Ray Conf-Vol. 7*, HE-4.4-4, 1985.

[13] J. Matthews, *A Heitler model of extensive air showers*,
Astroparticle Physics **22** (2005) 387.

[14] T. Huege, *Radio detection of cosmic ray air showers in the digital era*,
Physics Reports **620** (2016) 1.

[15] F. Kahn and I. Lerche, *Radiation from cosmic ray air showers*,
Proceedings of the Royal Society of London. Series A. Mathematical and Physical Sciences **289** (1966) 206.

[16] O. Scholten, K. Werner and F. Rusydi, *A macroscopic description of coherent geo-magnetic radiation from cosmic-ray air showers*,
Astroparticle Physics **29** (2008) 94.

[17] G. Askaryan, *Excess negative charge of an electron-photon shower and the coherent radio emission from it*,
Journal of Experimental and Theoretical Physics Letters **41** (1961).

[18] H. Schoorlemmer, *Tuning in on cosmic rays: polarization of radio signals from air showers as a probe of emission mechanisms*, 2012.

[19] T. Huege, *Radio detection of extensive air showers*,
Nuclear Instruments and Methods in Physics Research Section A **876** (2017) 9.

[20] K. D. Vries, A. van Den Berg, O. Scholten and K. Werner,
Coherent Cherenkov radiation from cosmic-ray-induced air showers,
Physical Review Letters **107** (2011) 061101.

[21] H. Schoorlemmer and W.R. Carvalho Jr, *Radio interferometry applied to the observation of cosmic-ray induced extensive air showers*,
The European Physical Journal C **81** (2021) 1120.

[22] The Pierre Auger Collaboration, *Depth of maximum of air-shower profiles at the Pierre Auger Observatory. I. Measurements at energies above* $10^{17.8}$ eV,
Physical Review D **90** (2014) 122005.

[23] I. Allekotte and A. Calvo, *Socioeconomic Impact of the Pierre Auger Observatory*,
Contribution to the 38th International Cosmic Ray Conference (ICRC 2025), 2025,
arXiv: 2507.10802 [astro-ph.IM],
URL: https://arxiv.org/abs/2507.10802.

[24] *Pierre Auger Observatory Detector Map*, URL:
https://www.eurekalert.org/multimedia/585347 (visited on 18/08/2025).

[25] H. Klages, *Enhancements to the Southern Pierre Auger Observatory*,
Journal of Physics: Conference Series **375** (2012) 052006.

[26] A. Castellina for the Pierre Auger Collaboration,
AugerPrime: The Pierre Auger Observatory Upgrade,
The European Physics Journal Web Conf. **210** (2019) 06002.

[27] The Pierre Auger Collaboration,
Observation of the suppression of the flux of cosmic rays above 4×10^{19} eV,
Physical Review Letters **101** (2008) 061101.

[28] M. Weitz for the Pierre Auger Collaboration,
"Adding interferometric lightning detection to the Pierre Auger Observatory",
Journal of Physics: Conference Series, vol. 2985, 1, Contribution to the Atmospheric Monitoring for High Energy Astroparticle Detectors 2024 (AtmoHEAD 2024),
IOP Publishing, 2025.

[29] M. Gottowik, *Recent Highlights from the Auger Engineering Radio Array*,
Contribution to the 38th International Cosmic Ray Conference (ICRC 2025), 2025,
arXiv: 2507.08510 [astro-ph.HE],
URL: https://arxiv.org/abs/2507.08510.

[30] J. Kelley,
Data acquisition, triggering, and filtering at the Auger Engineering Radio Array,
Nuclear Instruments and Methods in Physics Research Section A **725** (2013) 133.

[31] H. Schoorlemmer et al., "Radio Interferometry applied to air showers recorded by the Auger Engineering Radio Array",
38th International Cosmic Ray Conference (ICRC2023)-Cosmic-Ray Physics,
Sissa Medialab, 2024.

[32] The Pierre Auger Collaboration, *Nanosecond-level time synchronization of autonomous radio detector stations for extensive air showers*,
Journal of Instrumentation **11** (2016) P01018.

[33] F. Schröder, "A Reference Beacon for the Auger Engineering Radio Array",
Instruments and Methods for the Radio Detection of High Energy Cosmic Rays,
Springer, 2012.

[34] D. Schmidt, *AugerPrime: Status and first results*,
Contribution to the 38th International Cosmic Ray Conference (ICRC 2025), 2025,
arXiv: 2508.08056 [astro-ph.IM],
URL: https://arxiv.org/abs/2508.08056.

[35] A. Travaini, Private communication, 2025.

[36] D. Charrier for the CODALEMA Collaboration,
Antenna development for astroparticle and radioastronomy experiments,
Nuclear Instruments and Methods in Physics Research Section A **662** (2012) 142.

[37] D. Charrier for the CODALEMA Collaboration, "Design of a low noise, wide band, active dipole antenna for a cosmic ray radiodetection experiment",
2007 IEEE Antennas and Propagation Society International Symposium, 2007 4485.

[38] *The Butterfly Antennas*,
URL: https://codalema.in2p3.fr/instruments/butterfly/ (visited on 25/08/2025).

[39] S. Heidbrink, Private communication, 2025.

[40] C. Rühle, *Entwicklung eines schnellen eingebetteten Systems zur Radiodetektion kosmischer Strahlung*, (2013).

[41] M. Lipiński, T. Włostowski, J. Serrano and P. Alvarez, "White rabbit: A PTP application for robust sub-nanosecond synchronization", *2011 IEEE International Symposium on Precision Clock Synchronization for Measurement, Control and Communication*, IEEE, 2011 25.

[42] *WR-LEN User Manual*, Available at `https://safran-navigation-timing.com/wp-content/uploads/2024/05/WR-LEN-User-Manual-rev4.pdf`, SAFRAN, 2024.

[43] E. T. de Boone, Private communication, 2025.

[44] L. Eggert and G. Fairhurst, *Unicast UDP Usage Guidelines for Application Designers*, 2008, URL: `https://www.rfc-editor.org/info/rfc5405`.

[45] E. Por, M. Van Kooten and V. Sarkovic, *Nyquist–Shannon sampling theorem*, **1** (2019) 1.

[46] *Butterworth digital and analoge Filter design*, Avaiblabel at `https://docs.scipy.org/doc/scipy/reference/generated/scipy.signal.butter.html`, The SciPy community, 2008.

Acknowledgements

While working on this thesis, I received a great amount of support from a wide variety of people. First, I would like to thank Prof. Dr. Markus Cristinziani, who enabled me to write this thesis in the field of experimental astroparticle physics, and has repeatedly inspired interesting discussions. I am also grateful to have been involved in the construction of the new ATLAS pixel detector during my studies as a student research assistant. Furthermore, I would like to thank Prof. Dr. Markus Risse for kindly agreeing to be the second reviewer of this thesis.

Special thanks go to Dr. Qader Dorosti, who supervised my bachelor's thesis, as well as my master's thesis, and put a lot of effort into the project to make it successful. He also taught me a lot during my studies, even outside of lectures, as part of my thesis, and while working as a student assistant. I am very grateful for that.

Furthermore, I would like to thank E.T. deBoone who shared the office with me in the last year and who gave me a lot of technical support, put a lot of effort into the work with the AERA digitizers and supported the measurement campaigns we conducted together.

I also want to thank the electronic lab of the physics department, headed by Dr. Michael Ziolkowski. The team provided great support, especially when working in the laboratory and conducting measurement campaigns.

A big thank you also goes to my fellow students, and especially to Nils Krengel, for all the hours we spent together in the many courses we attended together, and the support I got from him.

Last but not least, I would like to thank my family and my girlfriend, who have always been there for me and still are, for their great support over the last few years. You played a big part in helping me to complete my studies.

Thank you!